Aeropropulsive Performance Analysis of Axisymmetric Fuselage Bodies for Boundary-Layer Ingestion Applications

Baskaran, Pradeep; Corte, Biagio Della; Sluis, Martijn van; Rao, Arvind Gangoli

DOI
10.2514/1.J060362

Publication date
2022

Document Version
Final published version

Published in
AIAA Journal

AIAA JOURNAL
Vol. 60, No. 3, March 2022

Aeropropulsive Performance Analysis of Axisymmetric Fuselage Bodies for Boundary-Layer Ingestion Applications

Pradeep Baskaran,* Biagio Della Corte,† Martijn van Sluis,‡ and Arvind Gangoli Rao§
Delft University of Technology, 2629 HS Delft, The Netherlands

https://doi.org/10.2514/1.J060362

Boundary-layer ingestion (BLI) has been proposed as one of the novel airframe–engine integration technologies to reduce aircraft fuel consumption. The current numerical analysis involves the evaluation of the effect of fuselage design on the power consumption of a boundary-layer ingesting propulsor modeled as an actuator volume without nacelle. An axisymmetric fuselage model is used as a canonical case to study BLI in transonic flight conditions. The flowfield is investigated through the power balance and the exergy analysis methods. Results show that the fuselage geometry and flight conditions only have a minor effect on the BLI power saving benefit when compared to the effect on the drag power of the fuselage. This indicates that, for the range of fuselage geometries and flight conditions studied, the isolated fuselage drag can be used for a qualitative performance assessment of different fuselage designs even for BLI configurations. Also, the power saving results obtained based on the power balance and the exergy analysis methods show similar qualitative trends for the fuselage geometries and flight conditions considered. Furthermore, the BLI propulsor has a negligible effect on the upstream anergy generation rate. Turbulence and temperature gradients within the flow are the important reasons for the deterioration of the BLI propulsor performance as expected.

Nomenclature

$\dot{A}$	=	anergy generation rate
$\dot{A}_{\text{thm}}$	=	anergy generation rate due to thermal mixing
$\dot{A}_{\Phi}$	=	anergy generation rate due to viscous dissipation
b	=	local first streamtube circumference (as in MTFLOW)
$C_{\dot{A}S}$	=	overall coefficient of body-surface anergy generation rate
C_D	=	coefficient of drag
$C_{\mathcal{D}}$	=	shear-layer local coefficient of dissipation
C_f	=	shear-layer local skin-friction coefficient
C_P	=	coefficient of power
$C_{\Phi S}$	=	overall coefficient of body-surface viscous dissipation
c	=	chord (flat plate)
D	=	drag
$\mathcal{D}$	=	shear-layer local dissipation
d	=	diameter
$\dot{E}$	=	mechanical-energy deposition rate
$\dot{E}_a$	=	streamwise kinetic-energy deposition rate
$\dot{E}_p$	=	pressure work energy deposition rate
$\dot{E}_{\text{th}}$	=	thermal-energy deposition rate
$\dot{E}_v$	=	transverse kinetic-energy deposition rate
e	=	mass-specific internal energy
F_{wall}	=	body wall shear force
F_x	=	net force in x direction (axial direction)
h_0	=	mass-specific total enthalpy
$K_{\text{fo}}, K_{\text{af}}$	=	fuselage forebody and afterbody shape description parameters
k	=	medium thermal conductivity
L	=	length
M	=	Mach number
N_{crit}	=	natural transition-related exponent in e^N method
$\hat{\boldsymbol{n}}$	=	unit normal vector
P	=	propulsor power
P_K	=	mechanical-energy supply rate of propulsor
P_V	=	pressure–volume work rate
p	=	fluid static pressure
Re	=	Reynolds number
$r25$, $r50$, $r75$, $r100$	=	propulsor with radius 25, 50, 75, or 100% fuselage radius
S	=	area
s	=	mass-specific entropy
T	=	temperature
u', v'	=	velocity fluctuations in x and y directions (turbulence)
u, v, w	=	velocity components in x, y, z directions
V, $\boldsymbol{V}$	=	flow velocity value and vector
x, y, z or X, Y, Z	=	spatial coordinates or lengths
ΔC_{F_x}	=	net force count
δ	=	boundary-layer thickness
δ^*	=	boundary-layer displacement thickness
δ^{**}	=	boundary-layer density-flux thickness
$\dot{e}$	=	exergy flow
$\dot{e}_p$	=	exergy supply rate of propulsor
$\dot{e}_{\text{th}}$	=	thermal exergy flow
$\dot{e}_{\Phi}$	=	exergy flow due to viscous dissipation
θ	=	boundary-layer momentum thickness
θ^*	=	boundary-layer kinetic-energy thickness
ϑ	=	volume
μ or μ_l	=	fluid dynamic viscosity
μ_t	=	eddy viscosity
ρ	=	fluid mass density
τ_{wall}	=	wall shear stress
$\bar{\bar{\tau}}$	=	shear-stress tensor
Φ	=	viscous dissipation

Subscripts

baseline	=	baseline fuselage value
BLI	=	boundary-layer ingesting configuration value
case	=	case value

Received 2 December 2020; revision received 16 August 2021; accepted for publication 23 August 2021; published online 27 December 2022.

*M.Sc. Graduate, Faculty of Aerospace Engineering.
†Ph.D. Candidate, Faculty of Aerospace Engineering.
‡Researcher, Faculty of Aerospace Engineering.
§Associate Professor, Faculty of Aerospace Engineering; A.GangoliRao@tudelft.nl (Corresponding Author).

e	=	boundary-layer edge quantity
freestream	=	freestream ingesting configuration value
fuselage	=	fuselage value
iso	=	isolated body value
n	=	values tangential and normal to body surface (like x_n, y_n, u_n)
ppos	=	value over fuselage surface upstream of propulsor inlet face
propulsor	=	propulsor value
ref	=	reference value
$r25, r50, r75, r100$	=	value for propulsor with radius 25, 50, 75, or 100% fuselage radius, respectively
s	=	value over the fuselage surface (used for Φ_s and $\dot{A}_s$)
TE	=	value at the body trailing edge
w	=	value over the body wake
∞	=	freestream value

I. Introduction

THE aviation industry is set out to cut down aircraft fuel consumption, noise, and emissions. A few of the ambitious goals set include the NASA N+3 program, which aims for 70% fuel burn, 75% landing and takeoff NO_x emissions, and 71 dB noise reductions by 2035 [1]. Also, the targets set by the Advisory Council for Aeronautical Research in Europe (ACARE) in the Flightpath 2050 report aim for a 75% CO_2 emissions per passenger kilometer, 90% NO_x, and 65% noise reductions by 2050 [2]. Thus, novel aircraft technologies are being investigated to achieve these goals.

Boundary-layer ingestion (BLI) and wake ingestion (WI) are concepts that, respectively, involve the use of low-momentum viscous flow in the boundary layer or the wake flow from an airframe surface instead of the freestream flow for propulsion. Several research aircraft configurations have been defined, which use BLI/WI along with freestream ingestion (like STARC-ABL by NASA and the propulsive fuselage concept by Bauhaus Luftfahrt). Previous work has shown the potential of these concepts for reducing the power consumption of aircraft vehicles [3–7]. Boundary-layer ingestion and WI have already been studied and applied in the field of marine propulsion (e.g., in Refs. [8,9]). The benefit of operating a propeller in the wake of a body rather than in the freestream was already theorized by Betz [10]. A milestone theoretical analysis of WI is the work of Smith [3], in which the wake profile and the propulsor parameters are related to the achievable power benefit. In this work, an important performance metric called the power saving coefficient (PSC) is introduced as an attempt to compare wake ingesting and freestream propulsors. Moreover, classical analysis methods based on force and momentum equilibrium suffer from some limitations (e.g., in Ref. [11]). Namely, the propulsor and airframe forces (e.g., thrust and drag) cannot be univocally split and defined. The power balance method (PBM) provides a mechanical-energy analysis framework to identify the power sources and sinks in the flow [12]. Through the PBM, the following two mechanisms for the BLI or WI benefit were identified: first, the power carried by the ingested boundary layer or wake flow represents an input source for the propulsor efficiency [13]; second, the jet losses and wake dissipation are decreased with respect to a freestream ingesting configuration [7,14]. A similar analysis method based on the first and second laws of thermodynamics (an exergy-based method) can effectively be used to investigate both the mechanical and thermal effects involved in BLI configurations [15], which especially become important for transonic flight conditions.

Many detrimental airframe–propulsor interaction phenomena can lead to reduced power benefits. In particular, previous studies have highlighted the increase in airframe drag due to the integrated propulsor [7], reduced propulsor efficiency due to inflow distortion [16–18], and the effect of shock waves on the airframe surface [19].

Experimental analyses serve as a proof of concept for the possible power benefit of BLI configurations. An example is the D8 aircraft, where promising power saving results (8.6% for cruise condition) were obtained [5]. It should be noted that the power savings, as reported in [5], are more relevant when considering the whole aircraft. Moreover, the BLI and WI power benefit was experimentally investigated using different bodies of revolution [6,20] also. A power saving of close to 25% is found for subsonic equilibrium conditions in these investigations.

The computational fluid dynamics (CFD) analyses in the literature cover the important effects involved in BLI/WI systems. They also discuss some methods to perform optimization and sensitivity analysis on computationally intensive frameworks, like Reynolds-averaged Navier–Stokes (RANS) CFD [21]. Elmiligui et al. [22] present an analysis of three different fuselage–propulsor configurations and the associated power savings. Bluementhal et al. [23], on the other hand, present a strategy to optimize the fuselage geometry by changing the pressure fields and adapting the physical geometry accordingly. The modeling of the configurations in the literature ranges from axisymmetric fuselage models with steady flow [22] to 3-D steady flow models [16], including wings. Kenway and Kiris [16] address the flow distortion aspect of BLI by optimizing the fuselage geometry in a 3-D RANS simulation framework. Gray et al. [21], on the other hand, address the aeropropulsive coupling using a sensitivity analysis of an actuator-disk pressure ratio (PR) modeled to represent a fan at the end of a fuselage. Because the fuselage of the aircraft is identified to be the most important aerodynamic body for BLI in a tube–wing aircraft configuration (due to the highest length in the flow direction), its design needs to be extensively studied. Although previous studies have addressed this to some extent, a more detailed analysis focusing on the use of contemporary theoretical methods combined with a CFD framework to analyze the fuselage would be useful, which is the objective of the present study (based on the thesis by Baskaran [24]). Thus, in the present study, an axisymmetric fuselage model is used along with an actuator volume propulsor model to study the effects of the fuselage design, the propulsor size and position, and the flight speed on BLI/WI. This involves the use of an Euler–integrated boundary layer theory (IBLT) solver and a RANS solver for the exploration. The benefits and limitations of each of the solvers are also identified.

II. Theory of Analysis Methods

This section summarizes the two methods used to analyze BLI. The control volume (CV) used for the analysis is shown in Fig. 1.

A. Power Balance Method

The PBM is a mechanical-energy analysis framework, which can be used to analyze any closely integrated configuration in different flow conditions [12]. The general formulation can be given for level flight as

$$P_V + P_K = \dot{E} + \Phi - F_x V_\infty \tag{1}$$

where the left-hand terms represent the power sources, whereas the right-hand terms represent the power sinks. In particular, $\dot{E}$ is the power outflow through the volume boundaries, Φ is the mechanical power lost (increasing the fluid internal energy) in the CV due to viscous dissipation, and $F_x V_\infty$ is the power due to the net force.

These terms can be expressed as integrals of flowfield variables, as explained by Drela [12]. The P_K term represents the net mechanical-energy outflow from the propulsor, and it is expressed as

$$P_K = \iint_{\mathrm{BS}} -\left[(p - p_\infty) + \frac{1}{2}\rho(V^2 - V_\infty^2)\right]\boldsymbol{V}\cdot\hat{n}\,\mathrm{d}S \tag{2}$$

It should be noted that this equation is not used to obtain P_K in the RANS studies of the current paper. Instead, power is calculated on the basis of the source terms (momentum and energy) added to the propulsor volume.

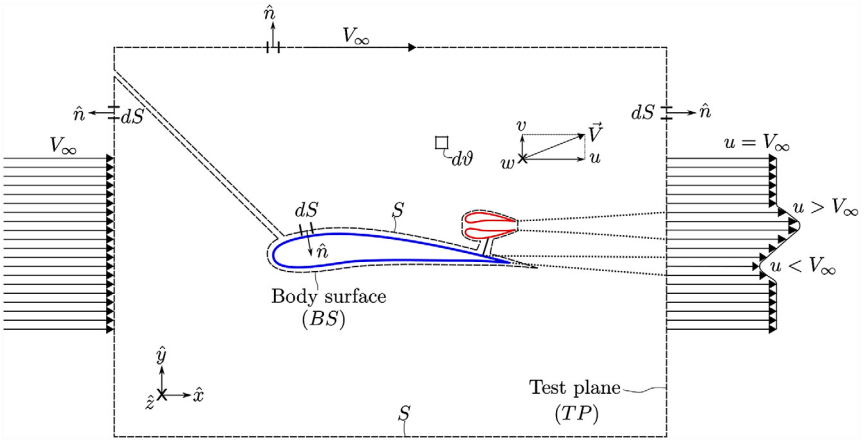

Fig. 1 Control volume defined for power balance and exergy analysis.

Next, P_V is the power spent through the expansion or compression against the atmospheric pressure, which is nonnegligible in compressible flows:

$$P_V = \iiint_{\mathrm{CV}} (p - p_\infty) \nabla \cdot \boldsymbol{V} \, \mathrm{d}\vartheta \tag{3}$$

Furthermore, $\dot{E}$ can be split into several contributions as follows [assuming test plane (TP) is normal to the freestream velocity]:

$$\dot{E} = \dot{E}_a + \dot{E}_v + \dot{E}_p = \iint_{\mathrm{TP}} \frac{1}{2}\rho(u - V_\infty)^2 u \, \mathrm{d}S + \iint_{\mathrm{TP}} \frac{1}{2}\rho(v^2 + w^2) u \, \mathrm{d}S + \iint_{\mathrm{TP}} (p - p_\infty)(u - V_\infty) \, \mathrm{d}S \tag{4}$$

$\dot{E}$ includes the mechanical-energy fluxes through TP associated with the axial and transverse velocity components, along with the pressure work rate. In an isolated body analysis, $\dot{E}$ is calculated in the TP located at the trailing edge (TE) and would give an indication of the power that can be saved by an ideal wake propulsor, which has no jet loss and does not change the upstream flowfield. However, it should be noted that this is valid only if the thermal and compressibility effects are negligible (at low speeds). Otherwise, the value of $\dot{E}$ will usually become negative close to the body TE and would no longer be directly useful to quantify the power saving.

Φ represents the dissipation of mechanical power into heat due to viscous shear stresses:

$$\Phi = \iiint_{\mathrm{CV}} (\bar{\bar{\tau}} \cdot \nabla) \cdot \boldsymbol{V} \, \mathrm{d}\vartheta \tag{5}$$

Finally, the term $F_x V_\infty$ represents the power due to the net force. For an isolated body, this would equal the drag power DV_∞. It should be noted that, in the present paper, the equation for F_x in [12] is not used. Instead, it is obtained by integrating the pressure and shear stresses over the body and based on the momentum source values added to the propulsor volume.

B. Exergy Analysis Method

The analysis of closely integrated aircraft configurations requires clarity when handling the thermal effects, especially in the transonic flight regime. This is achieved by the exergy analysis method (EAM) [15]. This method could be looked at as an extension of the PBM to include the details of thermal effects in the flow. The main advantage is that the theoretical power that can be saved from a given boundary layer or wake flow can be predicted. Unlike mechanical power, the usability of thermal power is restricted by the second law of thermodynamics. This leads to the definition of exergy, which consists of the mechanical energy and the thermal energy that is theoretically available for performing work. The general formulation of the exergy analysis for an adiabatic airframe is

$$\dot{\varepsilon}_p = \dot{E} + \dot{\varepsilon}_{\mathrm{th}} + \dot{A} - F_x V_\infty \tag{6}$$

The left-hand term $\dot{\varepsilon}_p$ represents the exergy supplied by the propulsor, and it is given by

$$\dot{\varepsilon}_p = -\iint_{\mathrm{BS}} \rho(h_0 - h_{0,\infty})(\boldsymbol{V} \cdot \hat{n}) \mathrm{d}S + \iint_{\mathrm{BS}} T_\infty \rho(s - s_\infty)(\boldsymbol{V} \cdot \hat{n}) \mathrm{d}S \tag{7}$$

On the right-hand side of Eq. (6), $\dot{E}$ is the mechanical-exergy deposition rate, which is the same as the mechanical-energy deposition rate $\dot{E}$ in Eq. (4).

In addition, the thermal-exergy deposition rate $\dot{\varepsilon}_{\mathrm{th}}$ is defined as (assuming TP is normal to the freestream velocity)

$$\dot{\varepsilon}_{\mathrm{th}} = \dot{E}_{\mathrm{th}} + \iint_{\mathrm{TP}} p_\infty u \, \mathrm{d}S - \iint_{\mathrm{TP}} T_\infty \rho(s - s_\infty) u \, \mathrm{d}S \tag{8}$$

where $\dot{E}_{\mathrm{th}}$ is the thermal-energy deposition rate

$$\dot{E}_{\mathrm{th}} = \iint_{\mathrm{TP}} \rho(e - e_\infty) u \, \mathrm{d}S \tag{9}$$

Finally, $\dot{A}$ is the anergy generation rate given by (assuming TP is normal to the freestream velocity)

$$\dot{A} = \dot{A}_\Phi + \dot{A}_{\mathrm{thm}} = \iint_{\mathrm{TP}} T_\infty \rho(s - s_\infty) u \, \mathrm{d}S = \int\int\int_{\mathrm{CV}} \frac{T_\infty}{T} (\bar{\bar{\tau}} \cdot \nabla) \cdot \boldsymbol{V} \, \mathrm{d}\vartheta + \iiint_{\mathrm{CV}} \frac{T_\infty}{T^2} k (\nabla T)^2 \, \mathrm{d}\vartheta \tag{10}$$

The anergy represents the share of energy contained in the system, which cannot be converted to useful work. The decomposition of the anergy generation rate has been obtained as the sum of the anergy rate due to viscous dissipation $\dot{A}_\Phi$ and thermal mixing $\dot{A}_{\mathrm{thm}}$. The heat due to viscous dissipation can also act as a power source, and it is possible to define an exergy due to viscous dissipation as

$$\dot{\varepsilon}_\Phi = \iiint_{\mathrm{CV}} \left(1 - \frac{T_\infty}{T}\right) (\bar{\bar{\tau}} \cdot \nabla) \cdot \boldsymbol{V} \, \mathrm{d}\vartheta \tag{11}$$

Also, the anergy generation rate splitting is made possible by the application of eddy-viscosity model in mean entropy production of Moore and Moore [25] as mentioned in [15].

The EAM can be related to the PBM using the following equation:

$$\dot{A} - \Phi = \dot{A}_{\text{thm}} - \dot{\varepsilon}_{\Phi} \tag{12}$$

C. Performance Metrics

The analysis methods discussed earlier allow the definition of different performance metrics. The PSC as defined by Smith [3] is given by

$$\text{PSC}_{\text{actual}} = \frac{P_{\text{freestream}} - P_{\text{BLI}}}{P_{\text{freestream}}} \tag{13}$$

where $P_{\text{freestream}}$ and P_{BLI} are the propulsive power required for a given net axial force with a freestream ingesting and BLI propulsors, respectively. In the present study, the freestream propulsor is chosen to have the same dimensions as the respective BLI propulsor.

It should be noted that BLI/WI configurations have been observed to perform even better than ideal non-BLI propulsors [10]. Thus, instead of defining a specific nonideal freestream propulsor for quantifying BLI propulsor performance, an ideal freestream propulsor can be used (whose power consumption would be DV_{∞}). Thus, a strict definition of PSC can be given as

$$\text{PSC}_{\text{strict}} = \frac{DV_{\infty} - P_{\text{BLI}}}{DV_{\infty}} \tag{14}$$

which is more convenient for comparing different BLI or WI configurations, as the reference propulsor power requirement is readily defined by the isolated body aerodynamics (DV_{∞}).

Moreover, an aerodynamic body could be analyzed without propulsor operation, and the power that can be saved using its boundary layer or wake could be obtained. This power is the maximum power benefit achievable through an ideal BLI propulsor, which completely fills the wake or boundary layer and at the same time does not affect the upstream flow [12]. Then, a BLI/WI PSC can be defined directly for an isolated body analysis as follows:

$$\text{PSC}_{\text{ideal}} = \left(\frac{DV_{\infty} - \Phi}{DV_{\infty}}\right)_{\text{TE}} = \left(\frac{\dot{E} - P_V}{DV_{\infty}}\right)_{\text{TE}} \tag{15}$$

This definition is not satisfactory, as the thermal effects are not well addressed in the PBM at transonic speeds. For compressible flow regimes, another definition based on exergy method can be used as follows:

$$\text{PSC}_{\text{ideal}} = \left(\frac{DV_{\infty} - \dot{A}}{DV_{\infty}}\right)_{\text{TE}} = \left(\frac{\dot{\varepsilon}}{DV_{\infty}}\right)_{\text{TE}} \tag{16}$$

III. Flat-Plate Analysis

Analyzing the flow over a flat plate from the perspective of power balance is helpful in understanding certain important aspects of BLI/WI. The flow over an isolated body can be analyzed to get an indication of the power that can be saved using an ideal BLI propulsor. This was shown in the work by Drela [12]. Furthermore, the theoretical value (based on Blasius solution) of this recoverable power ($(\dot{E}/DV_{\infty})_{\text{TE}}$) for incompressible laminar flow over an isolated flat plate was shown to be ≈21% [12]. This could also be verified using CFD, as is presented in this section. Apart from this, the effect of closely integrating a propulsor with the flat plate (to attempt wake filling) is shown for an incompressible laminar-flow case using CFD. Finally, important power balance terms are also calculated for an incompressible turbulent flow case using $k-\omega-$SST and Spalart–Allmaras turbulence models. The postprocessing is done by calculating the power balance integrals using the interpolated flowfield result.

A. Laminar Flow over an Isolated Flat Plate

This subsection aims to computationally obtain the values of power balance terms for a simple case of incompressible laminar flow over a flat plate. The result is necessary for understanding the effect of BLI propulsor in the next subsection. A Reynolds number of 1×10^5 is chosen for the analysis. The boundary conditions and the CV used are given in Fig. 2.

The equation for power balance for this case with $P_K = 0$ (no propulsor) and $P_V = 0$ (flow incompressibility) is

$$\dot{E} + \Phi = DV_{\infty} \tag{17}$$

$$\dot{E}_a + \dot{E}_v + \dot{E}_p + \Phi = DV_{\infty} \tag{18}$$

The CV considered here is effectively 2-D. Assuming the plate leading edge to be the origin of the coordinate system with x parallel to the plate and y normal to the plate, the PBM integrals are listed as follows:

$$\dot{E}_a = 2\int_0^{Y_{\text{TP}}} \frac{1}{2}\rho(u - V_{\infty})^2 u \cdot \mathrm{d}y \tag{19}$$

$$\dot{E}_v = 2\int_0^{Y_{\text{TP}}} \frac{1}{2}\rho v^2 u \cdot \mathrm{d}y \tag{20}$$

$$\dot{E}_p = 2\int_0^{Y_{\text{TP}}} (p - p_{\infty})(u - V_{\infty}) \cdot \mathrm{d}y \tag{21}$$

$$\Phi = 2\int_0^{Y_{\text{TP}}} \int_{-X_{\text{LP}}}^{X_{\text{TP}}} \mu\left(\frac{\partial u}{\partial y}\right)^2 \cdot \mathrm{d}x \cdot \mathrm{d}y \tag{22}$$

The factor of 2 in the preceding integrals is due to the fact that the CV (as considered in Fig. 2) covers only the upper half and needs to be mirrored with respect to the flat plate to obtain the lower half as well.

The results of the power balance calculations are shown in Fig. 3. The calculated $\dot{E}$ term at the plate TE is found to be 22.95% of the drag power, which is the maximum power that a propulsor can save using BLI (if it does not affect the upstream flow). This is comparable to the value obtained from the Blasius-solution-based theoretical value of 21.39% (as mentioned in [12]).

B. Wake Filling for Laminar Flow over a Flat Plate

Using the isolated body analysis, it is possible to predict the possible power saving of a BLI configuration. However, the presence of a BLI propulsor also modifies the flow close to the body, leading to an increase in the value of integrated friction and pressure forces (seemingly causing an increase in drag) [7]. However, it was found that this does not necessarily mean an increase in body associated power dissipation [26]. Hall et al. [26], in fact, provide an explanation based on the boundary-layer shape factor as to when the pressure gradient created by a propulsor may actually cause an increased body

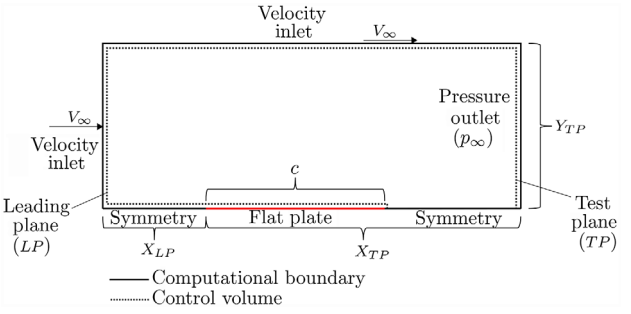

Fig. 2 Boundary conditions and CV definition for analyzing incompressible laminar flow over an isolated flat plate.

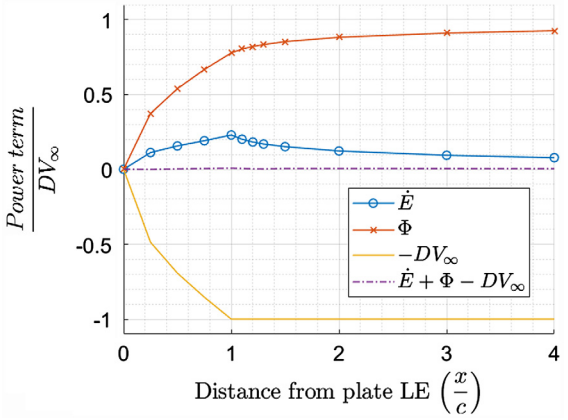

Fig. 3 Power balance results for laminar flow over an isolated flat plate; $F_x = D$; $Re = 1 \times 10^5$ (LE = leading edge).

power dissipation. It would be interesting at this point to analyze the effect of a simplified propulsor model on the BLI power benefit and to compare PSC_{strict} with the PSC_{ideal}. For this, the same flow conditions (laminar and incompressible with $Re = 1 \times 10^5$) as used in the isolated flat-plate (Sec. III.A) case are used. The propulsor is modeled by adding momentum sources in a rectangular region ($0.1c$ in length and $0.05c$ in height) of mesh behind the plate, as shown in Fig. 4. The propulsor height ($3.2 \times \delta$, assuming $\delta = 3 \times \delta^*$, which was obtained using Blasius solution for the isolated plate case) is selected to be greater than the boundary-layer thickness.

Next, as mentioned in Fig. 4, different momentum sources are added to the horizontal layers of the propulsor mesh to attempt a complete wake filling. The fluid dynamic viscosity μ inside the propulsor region is fixed to be zero to avoid viscous losses inside the propulsor. The momentum source values can be calculated using Bernoulli's theorem with a mechanical-energy addition term. For a propulsor as in Fig. 4, if each horizontal layer of cells has a cross-sectional area of S_{layer} and is responsible for a force (in x direction) delivery of F_{layer}, and if the pressure and x-velocity values in the first cell in each horizontal layer are p_{layer1} and u_{layer1}, respectively, then for achieving a freestream total pressure at the end of the propulsor, the following equation must be valid for any horizontal layer (neglecting the vertical velocity component):

$$p_{layer1} + \frac{1}{2}\rho u_{layer1}^2 + \frac{F_{layer}}{S_{layer}} = p_\infty + \frac{1}{2}\rho V_\infty^2 \tag{23}$$

Momentum source values in Fluent are applied per unit cell volume, and the x-momentum source per unit volume (m_{layer}) required in each cell layer can be calculated as

$$\frac{F_{layer}}{S_{layer}} = \frac{m_{layer}}{S_{layer}} \times \sum_{cellsinlayer} \text{Volume}_{cell} \tag{24}$$

$$m_{layer} \times \Delta X = p_\infty - p_{layer1} + \frac{1}{2}\rho(V_\infty^2 - u_{layer1}^2) \tag{25}$$

$$m_{layer} = \frac{p_\infty - p_{layer1} + \frac{1}{2}\rho(V_\infty^2 - u_{layer1}^2)}{\Delta X} \tag{26}$$

where ΔX is the distance through which the fluid is to be accelerated (or the total pressure change is to occur). The same value of ΔX will be used for all horizontal cell layers for simplicity. ΔX is calculated directly by equating plate drag with the propulsor thrust (and updated continuously during simulation iterations based on the updated value of plate drag). It should be noted that the net force F_x is obtained as the difference between the force due to integrated shear stresses over the plate and the force due to momentum sources added to the propulsor volume. Furthermore, the momentum sources added determine the respective energy source values (dot product of force due to the momentum source and local velocity), which determine P_K when summed over the propulsor volume. Because the flow is incompressible, energy sources need not be separately added.

The power balance results are given in Fig. 5. A Y_{TP} of $3c$ is used for the power balance calculations. It can be observed from the power balance result plots that the total drag power before the propulsor is higher than the total power required to propel the configuration. Of course, this is due to the use up of the wake power by the propulsor. The following observations are made:

1) The wake filler model performs well in terms of wake filling, leaving a very low propulsor jet power loss of 0.7% of the propulsor power P_K, which is comparable to the numerical error.

2) A PSC (PFC_{strict}) of 19.06% is obtained.

3) The drag increase compared to the isolated laminar-flow flat-plate configuration is 3.26%.

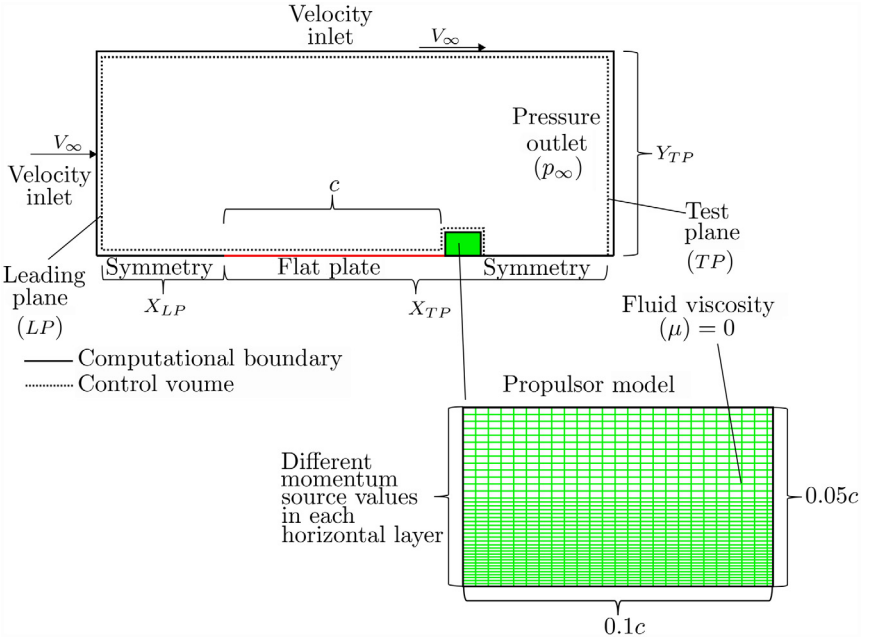

Fig. 4 Boundary conditions and CV definition for analyzing incompressible laminar flow over a flat plate with a BLI propulsor model.

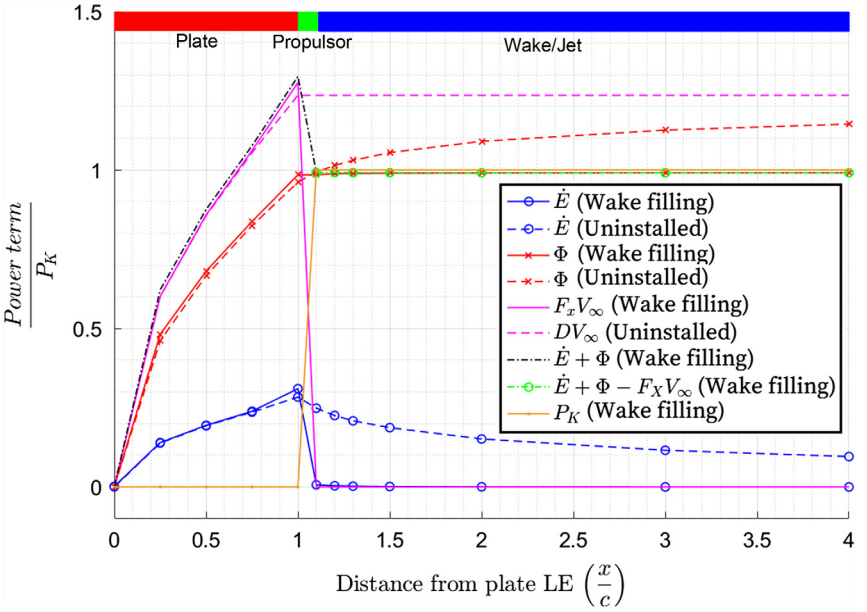

Fig. 5 Power balance results for laminar flow over a plate with propulsor; $F_x = 0$; $Re = 1 \times 10^5$.

4) The surface dissipation increase compared to the isolated flat plate is 2.44%. This can be noted in Fig. 5.

C. Turbulent Flow over an Isolated Flat Plate

Because most of the flow over a real aircraft tends to be turbulent, it becomes important to perform a simple comparison of commonly used turbulence models. A laminar model would also be compared alongside to mark the difference between laminar and turbulent cases. A Reynolds number of $Re = 10^7$ will be used for this study. Two turbulence models are compared, namely, k–ω–shear stress transport (SST) (Menter) and Spalart–Allmaras turbulence models. These were observed frequently in the literature [22,23,27]. The main aim is to compare the drag and the effective wake power. The difference in the power balance terms for the turbulence case when compared to the laminar case is for the viscous dissipation and the shear stress terms. The inclusion of Reynolds stress becomes important in the calculation. The wall shear force and viscous dissipation formulas are modified as follows (for Newtonian fluids):

$$F_{\text{wall}} = \iint_{\text{wall}} \left(\mu_l \left(\frac{\partial u}{\partial y} \right) - \rho \overline{u'v'} \right) \cdot \mathrm{d}S \tag{27}$$

$$\Phi = \int \int \int_{\text{CV}} \left(\mu_l \left(\frac{\partial u}{\partial y} \right)^2 - \rho \overline{u'v'} \left(\frac{\partial u}{\partial y} \right) \right) \cdot \mathrm{d}\vartheta \tag{28}$$

Because the considered turbulence models are eddy-viscosity models, the Reynolds stress term can be further simplified using Boussinesq's assumption (for incompressible flow):

$$-\rho \overline{u'v'} = \mu_t \left(\frac{\partial u}{\partial y} + \frac{\partial v}{\partial x} \right) \tag{29}$$

where the gradient $\partial u/\partial y$ is the dominant term, and the wall shear force and viscous dissipation can be expressed as

$$F_{\text{wall}} = \iint_{\text{wall}} (\mu_l + \mu_t) \left(\frac{\partial u}{\partial y} \right) \cdot \mathrm{d}S \tag{30}$$

$$\Phi = \iiint_{\text{CV}} (\mu_l + \mu_t) \left(\frac{\partial u}{\partial y} \right)^2 \cdot \mathrm{d}\vartheta \tag{31}$$

where μ_l is the laminar dynamic viscosity, μ_t is the eddy viscosity, and the x and y coordinates are taken tangential and normal to the body under consideration at any point. Next, the CV used is similar to the one shown in Fig. 2. The power balance results are given in Fig. 6.

It is clear from the power balance results that the power dissipation over the plate is higher in percentage (taken with respect to drag power DV_∞) for turbulent flow than for laminar flow. This results in a lower wake power availability ($(\dot{E}/DV_\infty)_{\text{TE}}$) for BLI applications. The important values of power balance terms are given in Table 1. (Drag coefficient is calculated using plate chord and unit width to obtain the reference area S_{ref}.) It is clearly observed from the results in Table 1 that the turbulent flow over the flat plate results in a higher drag as expected. Also, the results from both the investigated turbulence models are close to each other.

IV. Numerical Analysis and Optimization Setup for Axisymmetric Bodies

The possible power benefit from BLI is studied by analyzing the flow around different axisymmetric fuselage models. Two different CFD solvers are used, and the PBM and exergy methods are applied to the resulting flowfield (when applicable). The power required for cruise (no acceleration) for different fuselage geometries and flight conditions are compared and at the same time the power benefit of using a BLI or WI configuration is evaluated for the different cases.

The possible flight configuration for BLI is indeed a question that needs to be analyzed carefully. Different choices of novel aircraft concepts, like the D8 double bubble aircraft by the Massachusetts Institute of Technology, STARC-ABL by NASA, or the propulsive fuselage concept by Bauhaus Luftfahrt, are possible. Of these designs, the propulsive fuselage concept (or more generically fuselage-BLI) promises a high-power benefit [4]. Therefore, the current study will focus on such configurations, where BLI is applied on an axisymmetric body representative of an aircraft fuselage. The details of the geometry and flight conditions are chosen to be representative of a long-range commercial airliner. The underwing propulsors in the propulsive fuselage concept are not considered in this study, and the entire thrust is assumed to be produced by the BLI propulsor.

A. Methods

1. *Baseline Fuselage Geometry and Flight Conditions*

The baseline fuselage geometry, reported in Fig. 7, consists of an axisymmetric body representative of the fuselage of a long-range commercial aviation aircraft. The length of the body is 69 m with a maximum diameter of 6.205 m (with the diameter value unchanged for the whole study), resulting in a slenderness ratio of 11.12. The

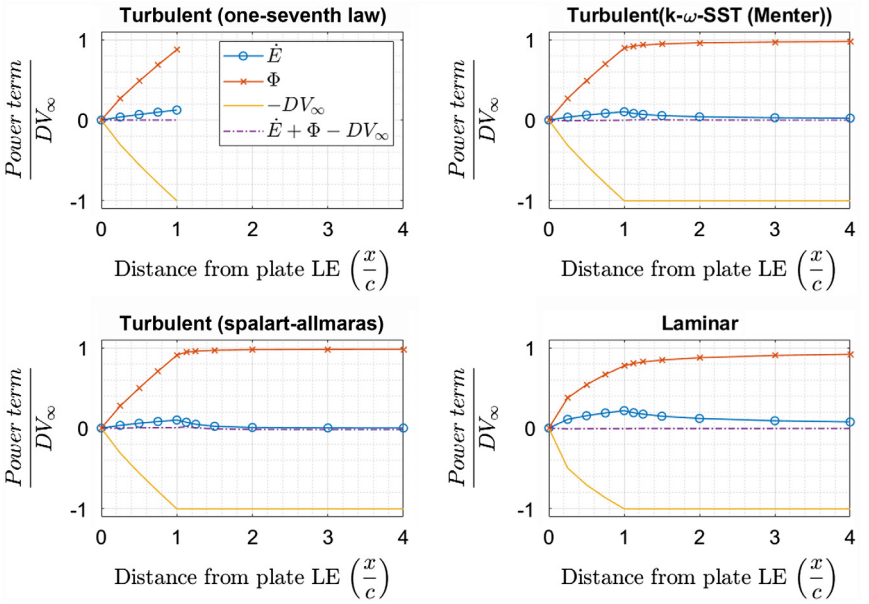

Fig. 6 Power balance plots of different models of flow over a flat plate; the legend in the first plot applies to all plots; $F_x = D$; $Re = 10^7$.

Table 1 Comparison of power balance results of different flow models for flow over a flat plate ($F_x = D$; $Re = 1 \times 10^7$)

Case	C_D	$\left(\frac{\dot{E}}{DV_\infty}\right)_{TE}$, %	$\left(\frac{\Phi}{DV_\infty}\right)_{TE}$, %
Turbulent (one-seventh law)	0.0064	12.50	87.50
Turbulent ($k-\omega-$SST)	0.005787	10.33	89.46
Turbulent (Spalart–Allmaras)	0.005989	10.07	90.59
Laminar	0.0008313	21.79	77.45

geometry is obtained from the ESDU I and II parametric shapes [28]. A particular shape can be obtained by fixing the control parameter K (details in Appendix A). In particular, the nose section is based on the ESDU I family ($K_{fo} = 0.9$) with a slenderness of 1.67, whereas the aft section is obtained from the ESDU II family ($K_{af} = 0.5$) with a slenderness of 2.5. The propulsor length (in the axial direction) is fixed at 1 m (unchanged for the whole study), and a baseline radial dimension is chosen to equal the fuselage cross-sectional area. The coefficients, like drag, etc., are defined based on the maximum fuselage frontal area S_{ref} as the reference.

The nominal flight conditions at which the simulations were carried out were chosen to be representative of the cruise conditions of a long-range commercial flight. The freestream Mach number was fixed to 0.80 (varied only during the flight speed design space study). An ambient pressure of $p_\infty = 23831.8$ Pa and a temperature of $T_\infty = 228.7$ K were fixed (close to flight level FL350 with ISA+10 temperature offset).

2. *Euler–IBLT Solver*

The design space exploration and the fuselage afterbody shape optimization are both done using MTFLOW [29]. This software is a combined Euler and integral boundary-layer theory solver focused on axisymmetric geometries. In addition, propulsor units can be simulated through actuator volume models. An example of a computational domain for a generic fuselage-BLI configuration in MTFLOW is shown in Fig. 8. MTFLOW assumes the real flow to be divided into an inviscid part, governed by the Euler equations, and a viscous part, governed by integral boundary-layer momentum and kinetic-energy equations. The transition to the turbulent boundary layer is modeled through the e^N method. The value of N_{crit} was fixed to 9 for all the simulations. This resulted in a transition location at around 3% of the fuselage length for the baseline fuselage geometry. Furthermore, as an example for baseline fuselage simulation, three meshes with the number of streamlines × number of streamwise grid points values of 45×145, 45×200, and 45×300 are used and respective drag coefficient values of 0.075378, 0.075259, and 0.075096 are obtained. The drag-coefficient values are very close as can be observed. The final meshes used have around the same number of grid points as that of the mesh with the grid of 45×300 for all the fuselage simulations. The computational domain extends approximately half the fuselage length (from the fuselage leading edge) in the upstream, twice the fuselage length (from the fuselage leading edge) in the downstream, and equal to the fuselage length in the normal directions.

The solver assumes no flowfield up to the displacement thickness δ^*. This affects the propulsor modeling, which can only operate on the inviscid flowfield. Therefore, the propulsor volume cannot entirely lie in the displacement thickness area. Moreover, the propulsor radius must be equal to or greater than the actual boundary-layer thickness δ. If this is not verified, the mass flow rate through the propulsor will be underpredicted when compared to the real physical flow, leading to errors. Furthermore, for propulsor modeling, the swirl change forcing is kept very low (so that the swirl velocity remains negligible) and the rotational speed value is made high for the actuator volume points. This allows to achieve the required axial momentum and the corresponding propulsor power. The inviscid flow equations in MTFLOW documentation [29] can be referred to for the details.

The boundary-layer equations are integrated across the boundary layer obtaining the von Kármán boundary-layer momentum integral and boundary-layer kinetic-energy integral (as obtained by Drela [30]) equations. These can be written for axisymmetric flows as [29]

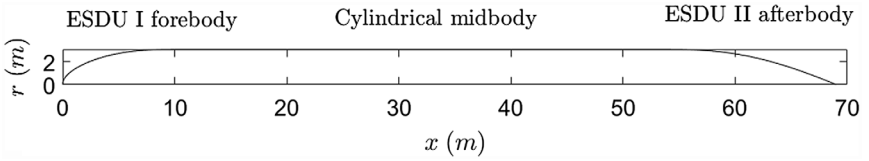

Fig. 7 Baseline fuselage geometry.

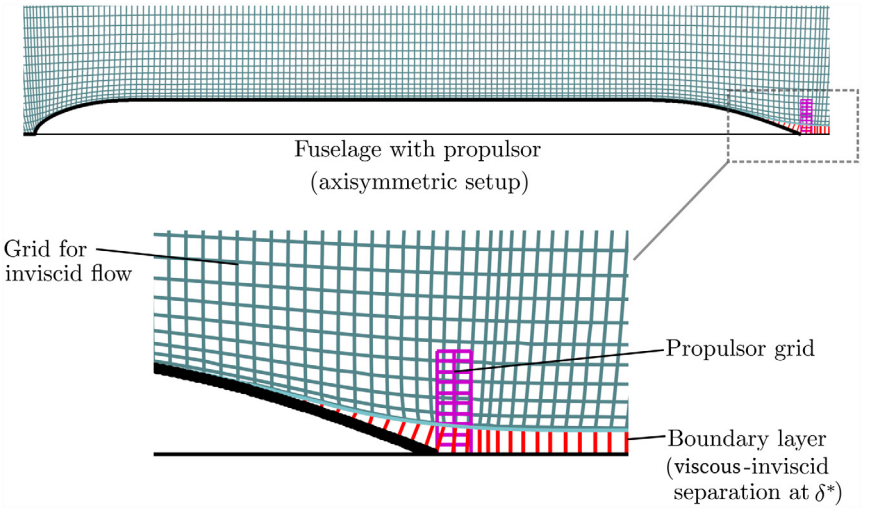

Fig. 8 Example flow domain and mesh in MTFLOW for Euler–IBLT simulations.

$$\frac{d(\rho_e u_e^2 \theta b)}{dx_n} = \rho_e u_e^2 b \frac{C_f}{2} - \rho_e u_e \delta^* b \frac{du_e}{dx_n} \tag{32}$$

$$\frac{d((1/2)\rho_e u_e^3 \theta^* b)}{dx_n} = \rho_e u_e^3 b C_{\mathcal{D}} - \rho_e u_e^2 \delta^{**} b \frac{du_e}{dx_n} \tag{33}$$

where $\rho_e u_e^2 \theta$ and $(1/2)\rho_e u_e^3 \theta^*$ are the momentum defect and the kinetic-energy defect, respectively. A form of these equations along with a shear lag equation as mentioned in [29] is used in MTFLOW. The dissipation coefficient in the integral kinetic-energy equation allows for directly obtaining the viscous dissipation in the flow.

3. *RANS Solver*

Steady-state RANS simulations were carried out to validate the main conclusions from Euler–IBLT solver results and to point out the possible shortcomings. The simulations were carried out through the commercial software package ANSYS, with Fluent as the flow solver. A sketch of the computational domain and boundary conditions used is shown in Fig. 9. The domain is divided into a laminar and a turbulent region to control the transition location on the fuselage contour. The transition location is matched to the one obtained in MTFLOW. The mesh spacing in proximity of the no-slip walls (fuselage body curve) was verified to produce $y^+ < 1$ throughout. The $k - \omega$–SST turbulence model is used [31]. The model option to account viscous heating and compressibility effects is switched on. Moreover, the Kato–Launder production model is enabled, with production limiter of 10^5. The molecular viscosity is calculated using the three-coefficient Sutherland law. The freestream turbulence intensity is fixed at 0.1% with a viscosity ratio of 2, based on Ref. [32]. Spatial discretization is done with a Green–Gauss cell-based method. A coupled pseudotransient solver algorithm is used, which allowed a fast and robust convergence, which was achieved with scaled residuals at least below 10^{-6}. Furthermore, as an example, for the baseline fuselage simulation (fully turbulent domain), three meshes with cell counts of 191,874, 422,154, and 608,584 are used, and respective drag coefficient values of 0.07288, 0.07282, and 0.07278 are obtained. The drag-coefficient values are very close as can be observed. The final mesh count used is around the same value as the mesh with 422,154 cells for all the fuselage simulations. The

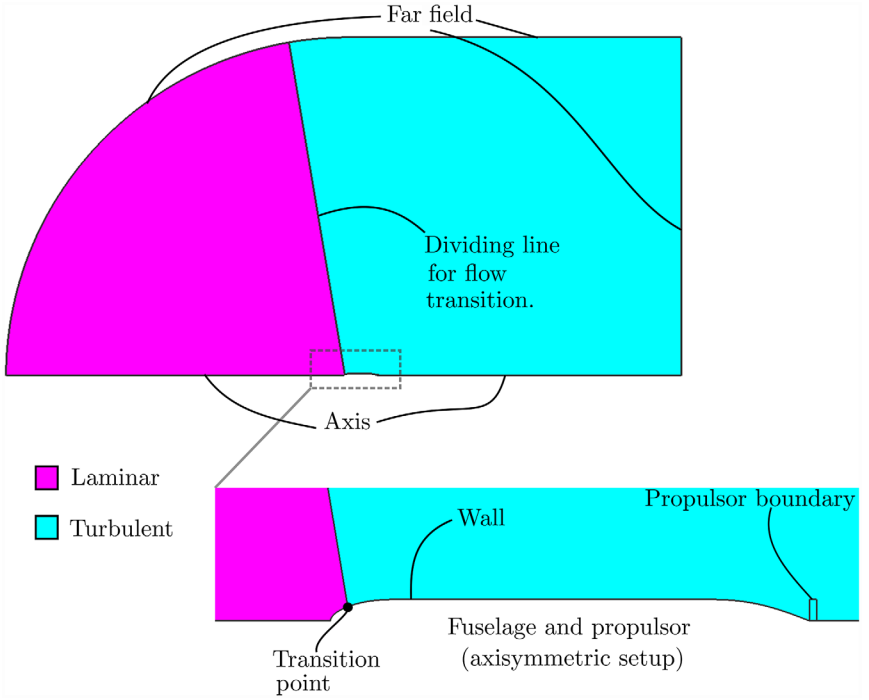

Fig. 9 Sketch of the flow domain and boundary conditions defined for the RANS simulations.

computational domain extends approximately 10 times the fuselage length (from the fuselage leading edge) in the upstream, downstream, and normal directions.

Furthermore, the BLI propulsor is modeled through the definition of an actuator volume, in which momentum and energy sources are added to the flow. The momentum sources are defined to produce a uniform pressure jump. The energy sources are calculated on the basis of the local velocity field and momentum addition. Mathematically, if F_{cell} is the local thrust force due to the momentum source, then the power source is calculated as $F_{\text{cell}}.u_{\text{cell}}$, where u_{cell} is the local fluid velocity (similar to that done in the work by Stokkermans et al. [33]). The power source in the cells in the propulsor volume is then summed to obtain the power. A schematic of the propulsor model is shown in Fig. 10. During the simulations, the propulsor thrust is constrained to be equal to the fuselage drag to obtain a zero net axial force. Postprocessing is done by calculating the required power balance and exergy integrals using the interpolated flowfield results. In the present paper, for isolated fuselage RANS studies, the drag D values are obtained by integrating the pressure and shear stresses over the fuselage body. For BLI configuration RANS studies, the integrated pressure and shear stresses over the fuselage body were subtracted from the force value corresponding to the momentum sources added to the propulsor volume.

B. Design Space Exploration

This study aimed to find the effect of fuselage geometry and flight conditions on the BLI power saving. The Euler–IBLT solver is used for the qualitative comparison of different configurations, as this requires less computational time. Some selected configurations are analyzed using the RANS solver to compare with the Euler–IBLT solver results. To isolate the effects of each parameter, a single sensitivity approach is used. This is achieved by sweeping a single parameter while all other parameters are kept fixed at the baseline values. The parameters, their baseline values, and their ranges are given in Table 2.

C. Fuselage Afterbody Optimization

Following the design space exploration, an optimization of the fuselage afterbody contour was performed. The optimization was done with the Euler–IBLT solver and used a gradient-based method with sequential quadratic programming. This was carried out separately for an isolated fuselage body and for a BLI configuration. For each case, a different objective function was defined.

For the isolated body, the objective was the minimization of the fuselage surface dissipation. For the BLI configuration, the net axial force was maximized for a fixed propulsor power. Figure 11 shows a sample geometry with the main constraints. The fuselage afterbody is divided into three parts, which include a leading section, a cylindrical midbody, and an exit section. The goal was to produce geometries typical of PFC-like designs (e.g., the NASA STARC-ABL [21] or the CENTRELINE PFC [34]). The leading section and exit section were parameterized using the ESDU II parametric curve family [28]. The normalized versions of the whole afterbody length, leading section length, cylindrical section length, leading section shape control parameter, exit section shape control parameter, and the position of propulsor inlet plane (for BLI) were included in the design vector. Geometrical constraints were imposed to mimic the design constraints that exist for a fuselage-BLI concept. In particular, the geometry was constrained so that the floor area of the leading section and the volume of the cylinder and exit section together would be constant. In fact, for a commercial aircraft, the floor area translates into seats and payload. Moreover, the housing of the propulsor subsystems (motor, fuel/power supply, cooling, etc.) in the aft cone section requires a certain volume. Also, the actuator volume, which models the fuselage propulsor, is constrained to lie only around the cylindrical section of the afterbody.

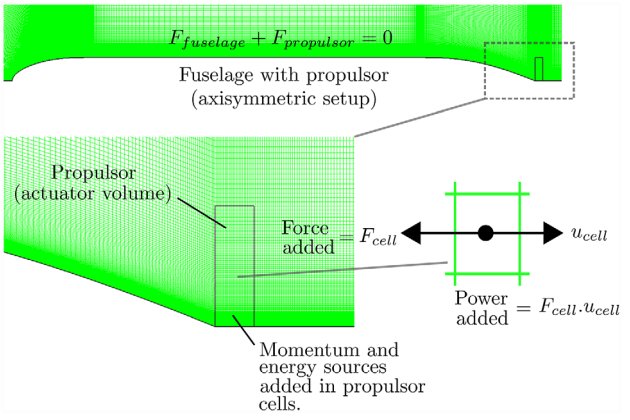

Fig. 10 Sketch of the propulsor model defined in ANSYS Fluent for the RANS simulations.

V. Results and Discussions

A. Analysis of Baseline Fuselage

This section investigates the performance of the baseline fuselage geometry in the flow conditions defined in Sec. IV.A.1. The flow around the fuselage was simulated using the RANS and Euler–IBLT solvers. The PBM and EAM results obtained from the flow simulations are presented in Fig. 12. The values of Φ, $\dot{\varepsilon}$, and $\dot{\varepsilon}_{\text{th}}$ are not calculated from the flowfield variables as integrals in case of RANS simulation. They are instead directly obtained from Eq. (1) or (6) as required using the values calculated for the other terms. Similarly, the $\dot{E} - P_V$ term is obtained using Eq. (1) in the Euler–IBLT calculations, in which the dissipation (Φ) is readily available from the simulation result.

It can be observed from the RANS results that the anergy generation rate value is higher than the viscous dissipation. This is because the PBM does not account for the thermal anergy rate $\dot{A}_{\text{thm}}$. This results in an overprediction of the power benefit for BLI applications for transonic flows when PBM is used. It can also be observed how the $\dot{E}$ term does not explicitly represent mechanical power unless the thermal exergy term $\dot{\varepsilon}_{\text{th}}$ becomes zero. On the contrary, the exergy is clearly the power available for saving. Next, the Euler–IBLT PBM results are off by a few percent when compared to RANS. This is expected to be due to the difference in modeling fluid flow in the solvers. It should be noted that the difference between kinetic-energy defect area $(1/2)\rho_e u_e^3 b\theta^*$ and viscous dissipation Φ in the Euler–IBLT calculations is not negligible (at least in the immediate wake of the fuselage) for the transonic flight under consideration.

Finally, the comparison of some important results from the RANS and Euler–IBLT solvers along with the drag prediction model from ESDU [35] is shown in Table 3. It can be observed that the results from the RANS simulation show excellent agreement with the results from the ESDU method, which indicates the quality of the RANS simulation results.

B. Design Space Exploration

1. *Fuselage Afterbody Shape*

The effect of the afterbody shape is studied by fixing all parameters except the afterbody shape control parameter K_{af}. The analyzed shapes are shown in Fig. 13. The results of the Euler–IBLT simulations for the isolated fuselage configuration are presented in Fig. 14. From the plot, it can be observed that the surface dissipation is lower for higher values of K_{af} (details in Fig. 13). Similarly, the drag of the body also decreases with increasing K_{af}. However, it can be noted that the change in ideal PSC with K_{af} is negligible.

An important complexity involved in the design of the fuselage for BLI application is the fact that the propulsor modifies the flowfield in its proximity, thereby changing certain important aerodynamic quantities. As observed in the flat-plate study, the presence of the propulsor tends to increase the friction drag and the plate surface viscous dissipation Φ_s. The shape of the body with which the propulsor is closely integrated and the flow conditions were found to affect this phenomenon as presented in the work by Hall et al. [26]. Hall et al. [26] explained a relationship between the boundary-layer shape

Table 2 Design space exploration parameters and values

Parameters	Isolated fuselage	BLI configuration ($F_x = 0$)
	Euler–IBLT values	
Afterbody shape parameter (K_{af})	0, 0.2, 0.5, 1, 2, 4, 6, 8, 10, 20, 50	0, 0.2, 0.5, 1, 2, 4, 6, 8, 10, 20, 50 (with r100 propulsor)
Afterbody slenderness $\left(\frac{L_{afterbody}}{d_{fuselage}}\right)$	2, 2.5, 3, 3.5, 4, 4.5, 5, 5.5, 6	2, 2.5, 3, 3.5, 4, 4.5, 5, 5.5, 6 (with r100 propulsor)
Fuselage slenderness $\left(\frac{L_{fuselage}}{d_{fuselage}}\right)$	5, 6, 7, 8, 9, 10, 11, 11.12, 12	5, 6, 7, 8, 9, 10, 11, 11.12, 12 (with r100 propulsor)
Flight Mach number	0.2, 0.3, 0.4, 0.5, 0.6, 0.7, 0.8, 0.85, 0.9, 0.95	0.2, 0.3, 0.4, 0.5, 0.6, 0.7, 0.8, 0.85, 0.9, 0.95 (with r100 propulsor)
Propulsor radius $\left(\frac{R_{propulsor}}{R_{fuselage}}\right)$	— —	0.85, 1, 1.25, 1.5, 1.75, 2
Propulsor position from fuselage leading edge $\left(\frac{x_{propulsor}-L_{fuselage}}{L_{afterbody}}\right)$	— —	−1, −0.75, −0.5, −0.25, 0, 0.25, 0.5, 0.75, 1, 2, 3, 4 (with equivalent r100 propulsor)
	RANS values	
Afterbody shape parameter (K_{af})	0, 50	0, 50 (with r50 and r100 propulsors)
Afterbody slenderness $\left(\frac{L_{afterbody}}{d_{fuselage}}\right)$	2.5, 6	2.5, 6 (with r50 and r100 propulsors)
Fuselage slenderness $\left(\frac{L_{fuselage}}{d_{fuselage}}\right)$	5, 11.12	5, 11.12 (with r50 and r100 propulsors)
Flight Mach number	0.2, 0.8, 0.9	0.2, 0.8, 0.9 (with r50 and r100 propulsors)
Propulsor radius $\left(\frac{R_{propulsor}}{R_{fuselage}}\right)$	— —	0.25, 0.5, 0.75, 1
Propulsor position from fuselage leading edge $\left(\frac{x_{propulsor}-L_{fuselage}}{L_{afterbody}}\right)$	— —	−0.75, 0 (with equivalent r25, r50, and r100 propulsors)

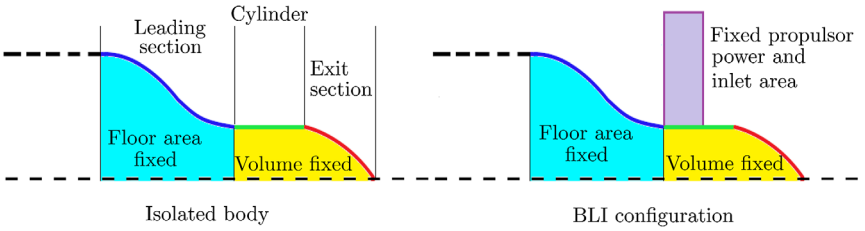

Fig. 11 Constraints on the fuselage configurations for the optimization study.

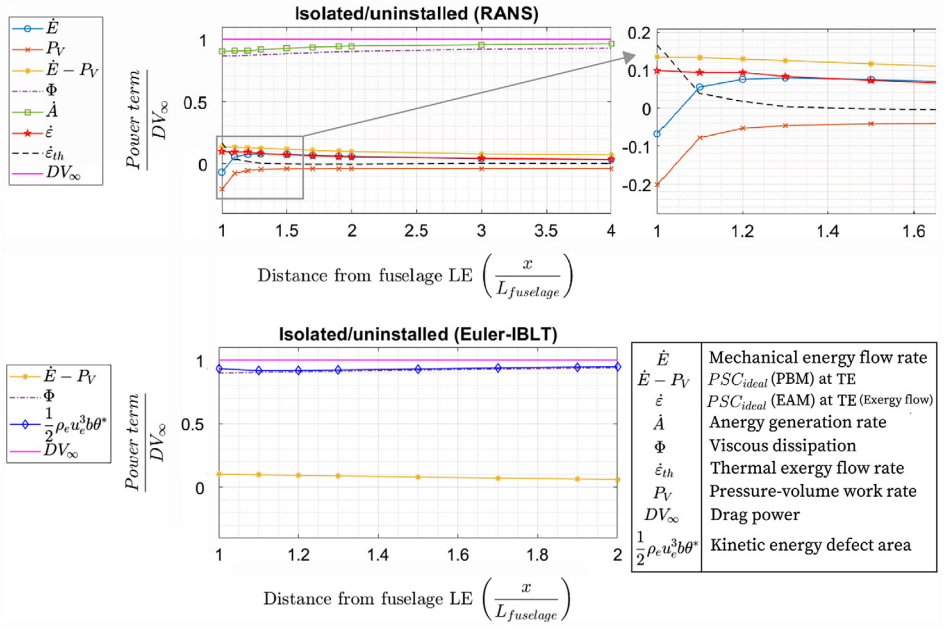

Fig. 12 Power balance and exergy analysis for the baseline fuselage geometry in baseline flight conditions; $F_x = D$; $M = 0.8$.

factor and the dissipation coefficient C_Φ. For turbulent flows, it was found that the static pressure changes created by a propulsor increased the boundary-layer edge velocity and decreased the local dissipation coefficient. Because of this, the static pressure change caused by the propulsor has negligible effect on the viscous dissipation upstream of it. (A maximum of 0.08% difference was observed for $K_{af} = 0$.) This effect can especially be seen if the local boundary-layer shape factor is greater than 1.4 or so [26].

The results of the analysis of the BLI powered fuselage are shown in Fig. 15 for different fuselage afterbody geometries. It can be

Table 3 Comparison of results from RANS, Euler–IBLT, and ESDU methods for the isolated baseline fuselage in the nominal flow conditions ($F_x = D$ and $M = 0.8$)

Quantity	ESDU 78019	RANS	Euler–IBLT	Difference (from RANS)
C_D	0.071715	0.071934	0.075096	0.31% (ESDU 78019) −4.40% (Euler–IBLT)
$\left(\frac{\dot{E}-P_V}{DV_\infty}\right)_{TE}$, %	— —	13.36	10.30	3.06
$\frac{\Phi_s}{DV_\infty}$, %	— —	86.64	89.70	3.06
$\left(\frac{\dot{\varepsilon}}{DV_\infty}\right)_{TE}$, %	— —	9.84	— —	— —
$\frac{\dot{A}_s}{DV_\infty}$, %	— —	90.16	— —	— —

observed that PSC_{strict} does not vary significantly for different afterbody shapes, similar to PSC_{ideal} for the isolated body case (Fig. 14). Moreover, the variation of the propulsive power is similar to the variation of the surface dissipation of the isolated fuselage. This hints at the fact that the isolated body viscous dissipation analysis can be effectively used to compare BLI configurations, at least for the qualitative comparison of different geometries in the present study.

The PBM and EAM were applied on the flow obtained through RANS simulations for selected fuselage shapes (isolated body analysis). For powered configurations, the power is known based on the applied energy sources, and the fuselage surface anergy is obtained based on the integral in the anergy method until TE. The results are presented in Tables 4 and 5. It can be noted from Table 4 that the maximum savable power as a percentage of drag power (the PBM-based and EAM-based PSC_{ideal}) does not change much between the two fuselage geometries. Furthermore, it can be observed from Table 5 that the fuselage surface anergy generation rate is not changed by the propulsor. Also, the drag coefficient C_D (obtained as the integrated pressure and viscous forces over fuselage body) is quite misleading for power consumption considerations, as the presence of the propulsor increases its value without affecting the surface anergy rate.

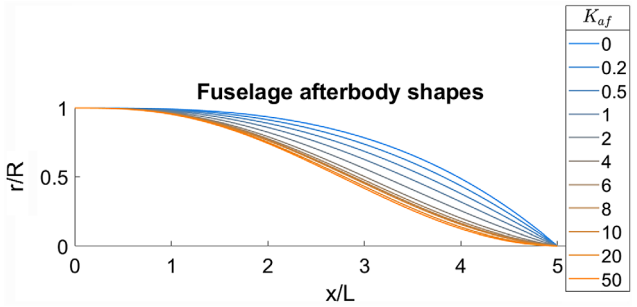

Fig. 13 Fuselage afterbody shapes for different values of K_{af} (based on ESDU II curve definition [28]).

2. *Propulsor Radius*

The analysis of propulsor-related parameters can be quite important to further understand BLI. The results for power saving are presented in Fig. 16. In Fig. 16, the smallest propulsor-to-fuselage-radius ratio used is 0.85. For values tried below 0.85 (like 0.75, 0.65, and 0.55), the PSC_{strict} values obtained are higher than the isolated body PSC_{ideal} value, and thus, these propulsor radii values are not used. It should be noted that the Euler–IBLT solver has limitations with regard to the size of the BLI propulsor that can be modeled when compared to the local boundary-layer thickness as mentioned in Sec. IV.A.2.

In addition, the RANS results for the baseline fuselage geometry (at 0.8 Mach) with different propulsor radii are given in Fig. 17. The PSC_{actual} values are calculated, simulating propulsors of the same respective radii for both BLI and freestream cases. Moreover, the drag values are calculated through the integral pressure and viscous forces only over the fuselage body. It can be observed that PSC_{strict} is highest (among the propulsor radii plotted) for a propulsor radius of $0.5 \times R_{fuselage}$. Moreover, the effect of the propulsors on the fuselage surface anergy generation rate was found to be negligible, as shown in Fig. 17. Because the momentum source is uniform in the propulsor volume and the entire propulsor thrust must equal the airframe drag, larger propulsors result in a lower pressure jump and vice versa. As a consequence, a lower amount of the boundary layer would be filled with increasing propulsor size to overcome the isolated fuselage surface anergy rate if the propulsor is larger than the boundary-layer thickness. On the other hand, propulsors smaller than the boundary layer ingest a fraction of the boundary layer, but achieve more filling due to the higher pressure jump required to obtain the required thrust. However, a small propulsor diameter results in more losses in the propulsor jet as jet velocity becomes faster than the freestream. This

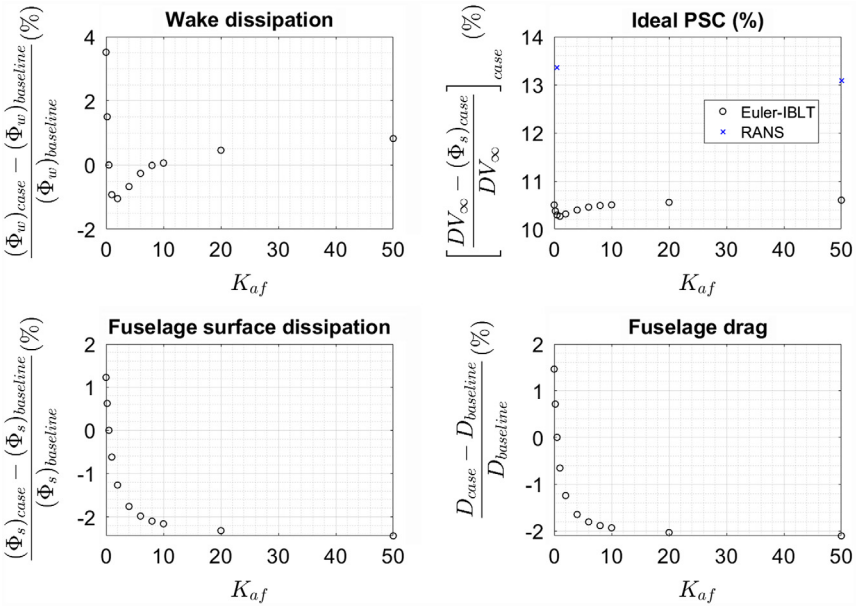

Fig. 14 Design space exploration results (Euler–IBLT) for different afterbody shapes (isolated body); $F_x = D$; $M = 0.8$.

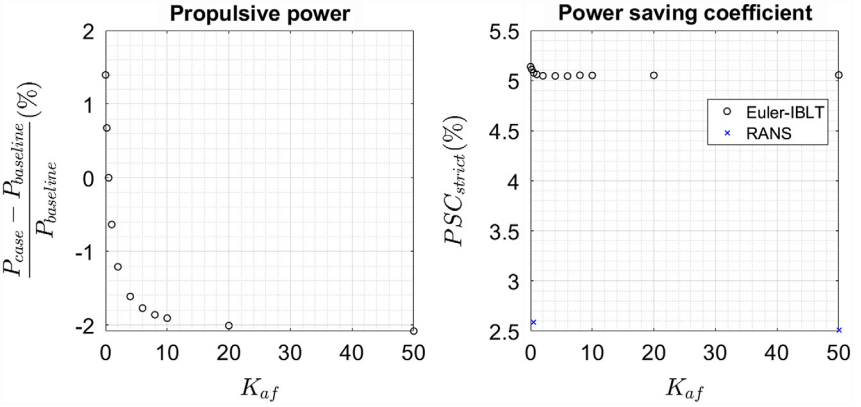

Fig. 15 Design space exploration results (Euler–IBLT) for different afterbody shapes (BLI configuration); $F_x = 0$; $M = 0.8$.

Table 4 Design space exploration results (RANS) for two afterbody shapes (isolated body) ($F_x = D$; $M = 0.8$)

Quantity	$K_{\text{af}} = 0.5$	$K_{\text{af}} = 50$	Difference
C_D	0.071934	0.070223	−2.38%
$C_{\Phi S}$	0.062320	0.061040	−2.05%
$C_{\dot{\text{A}}\text{S}}$	0.064854	0.063139	−2.64%
$\left(\frac{\dot{E}-P_V}{DV_\infty}\right)_{\text{TE}}$, %	13.36	13.08	−0.28
$\frac{\Phi_s}{DV_\infty}$, %	86.64	86.92	0.28
$\left(\frac{\dot{s}}{DV_\infty}\right)_{\text{TE}}$, %	9.84	10.09	0.25
$\frac{\dot{A}_s}{DV_\infty}$, %	90.16	89.91	−0.25

Table 5 Design space exploration results (RANS) for two afterbody shapes (BLI configuration) ($F_x = 0$; $M = 0.8$)

Quantity	$K_{\text{af}} = 0.5$	$K_{\text{af}} = 50$	Difference
$\frac{d_{\text{propulsor}}}{d_{\text{fuselage}}} = 1$			
C_D	0.079498	0.073697	−7.30%
C_P	0.070069	0.068464	−2.29%
$C_{\dot{\text{A}}\text{S}}$	0.064808	0.063228	−2.44%
$\text{PSC}_{\text{strict}}$, %	2.59	2.51	−0.08
$\frac{(\dot{A}_s)_{\text{case}}-(\dot{A}_s)_{\text{iso}}}{(\dot{A}_s)_{\text{iso}}}$, %	−0.0703	0.142	NA
$\frac{d_{\text{propulsor}}}{d_{\text{fuselage}}} = 0.5$			
C_D	0.08371	0.074758	−10.69%
C_P	0.066871	0.06524	−2.44%
$C_{\dot{\text{A}}\text{S}}$	0.064932	0.063348	−2.44%
$\text{PSC}_{\text{strict}}$, %	7.04	7.10	0.06
$\frac{(\dot{A}_s)_{\text{case}}-(\dot{A}_s)_{\text{iso}}}{(\dot{A}_s)_{\text{iso}}}$, %	0.12	0.33	NA

can especially be observed in Fig. 17 for the r25 propulsor. Some of the PRs, as shown in Fig. 17, may require more than one stage of compression.

3. *Propulsor Location*

Different design studies performed highlight the fact that the surface dissipation and surface anergy rate are unaffected by the addition of the propulsor aft of the fuselage in the considered flight regimes. However, an important concern in all the aforementioned studies is the fact that the propulsor installation location should be practically feasible. Even if one attaches a rotor without a nacelle at the aft part of the fuselage afterbody, some of the fuselage surface dissipation would still take place after the propulsor. Also, the available power (or exergy rate) in the flow upstream of the propulsor is different, depending on the location. The effect of the propulsor location was investigated by moving the location of the actuator volume along the length of the fuselage afterbody. The results of the Euler–IBLT simulations are reported in Fig. 18. It seems that the propulsors located on the fuselage body (before fuselage TE) do not achieve a good filling. The surface viscous dissipation was found to increase of up to 1.6% when the propulsor is located at the beginning of the fuselage afterbody. This is due to the effect of the propulsor jet, which interacts with the downstream fuselage boundary layer. Because the propulsor model in the Euler–IBLT solver operates in the inviscid flow, the value of the fuselage surface dissipation could be viewed as the fuselage surface viscous dissipation along with the effect of the propulsor jet on it (but excluding the explicit dissipation in the propulsor plume).

Finally, the results of the RANS simulations are shown in Fig. 19. The equivalent propulsor radius (mentioned in Fig. 19) represents the radius of a circle whose area equals the cross-sectional area of the propulsor intake. It should be noted that the anergy generation rate upstream of the fuselage TE also includes the anergy generated within the jet of the propulsor upstream of the fuselage TE (including dissipation within plume and any interaction effects with fuselage boundary layer).

4. *Observations and Comparison of Euler–IBLT and RANS Results*

The changes in various performance metrics as compared to the baseline case for different parameters are shown in Fig. 20. The results obtained display that for a qualitative comparison of the fuselage design (or flight conditions), both the RANS and the Euler–IBLT solvers are in good agreement. It can also be noted that the surface dissipation and the surface anergy rate results obtained from the RANS simulation are close. Moreover, the propulsive power values obtained in the BLI configurations follow the same trend as the surface dissipation and anergy rate in the isolated cases. This suggests that the isolated body performance metrics can be used for qualitative comparison of different BLI configurations (as also suggested by Hall et al. [26]).

The PSCs obtained through the Euler–IBLT and RANS simulations for selected cases are reported in Fig. 21. It can be observed that, except for the case at $M = 0.2$, the $((\dot{E} - P_V)/DV_\infty)_{\text{TE}}$ values do not match for the two solvers. Furthermore, the $\text{PSC}_{\text{strict}}$ values estimated through the Euler–IBLT simulations are higher than the value obtained through the RANS simulations. These discrepancies are probably due to differences in thermal effects modeling in the boundary layer in the Euler–IBLT solver when compared to the RANS solver. In fact, if the fluid thermal conductivity and viscous

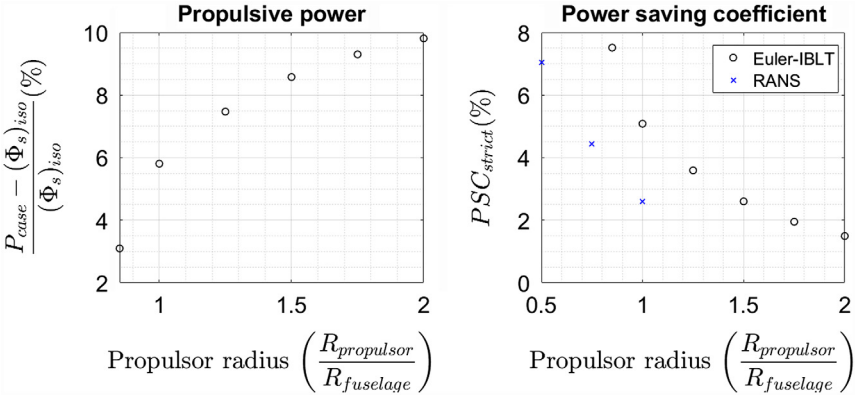

Fig. 16 Design space exploration results (Euler–IBLT) for baseline fuselage geometry with propulsors of different radii; $F_x = 0$; $M = 0.8$.

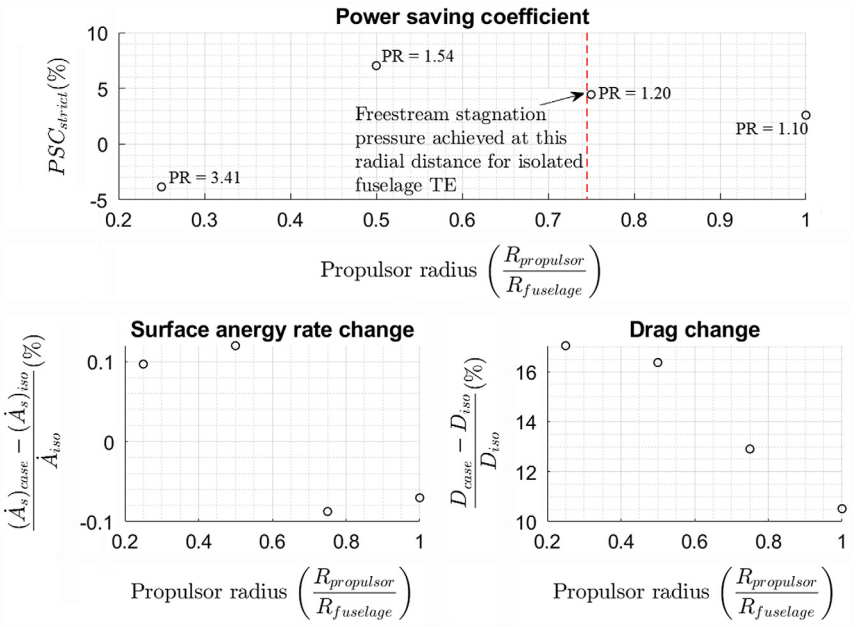

Fig. 17 Design space exploration results (RANS) for different propulsor radii; the propulsor PRs are also mentioned in the plot for PSC_{strict}; $F_x = 0$; $M = 0.8$.

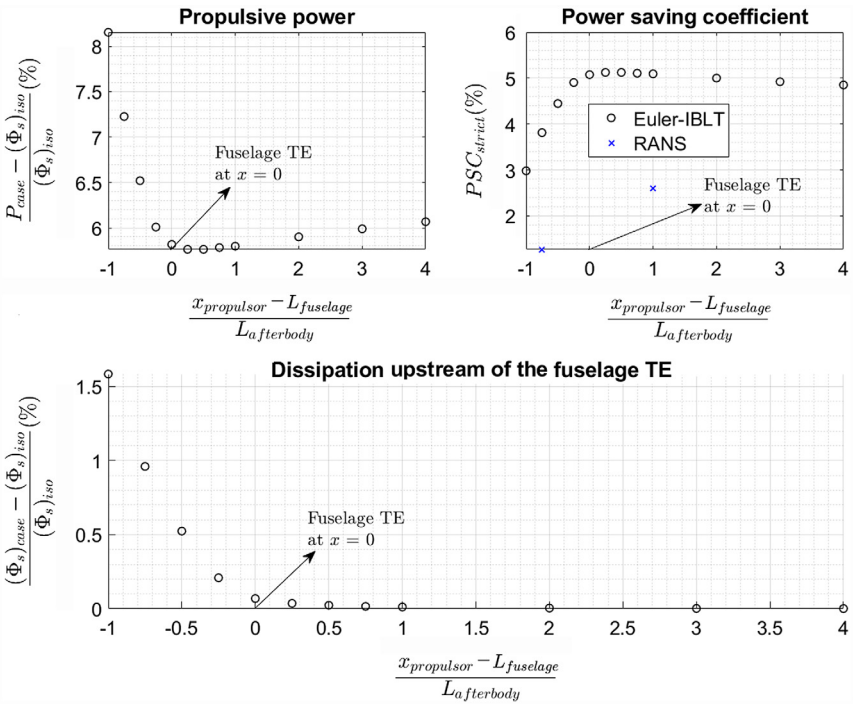

Fig. 18 Design space exploration results (Euler–IBLT) for baseline fuselage geometry with propulsor at different locations; $F_x = 0$; $M = 0.8$.

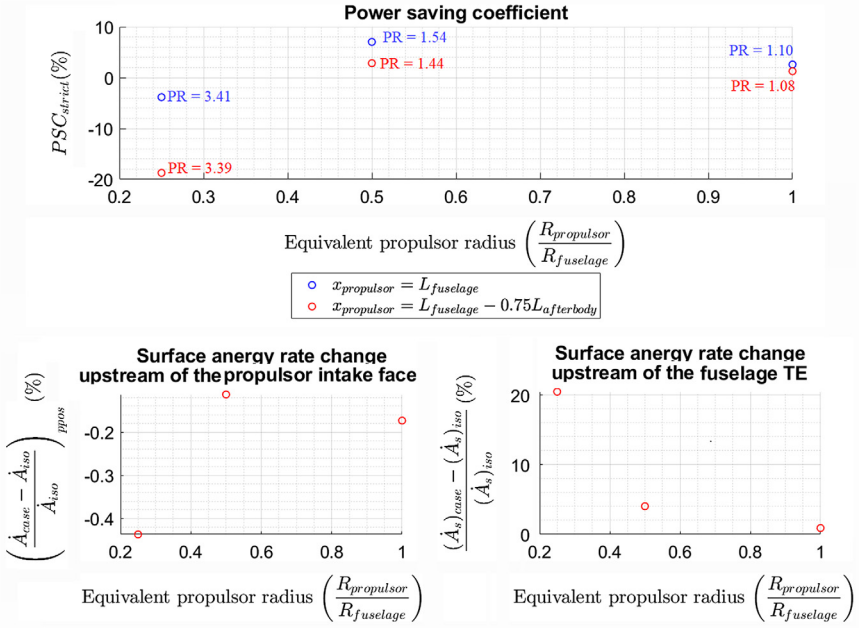

Fig. 19 Design space exploration results (RANS) for propulsor sizes located at a distance of $L_{\text{fuselage}} - 0.75L_{\text{afterbody}}$ from the fuselage leading edge; $F_x = 0$; $M = 0.8$.

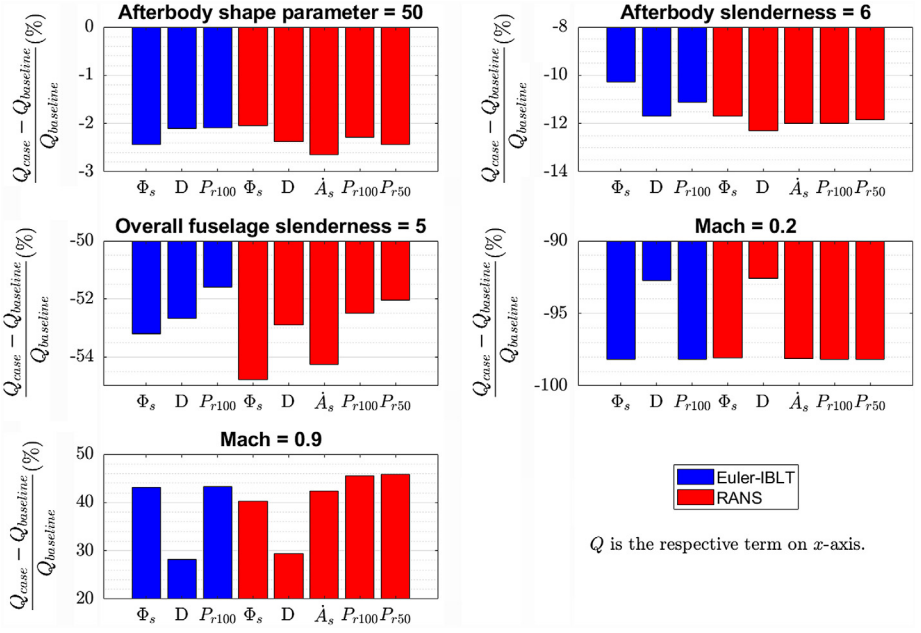

Fig. 20 Comparison of changes from the baseline configuration in power and momentum parameters (Euler–IBLT and RANS simulations).

heating are not modeled in the boundary layer, the difference between dissipation and anergy rate would be zero [details in Eq. (12)]. Because at higher Mach numbers the thermal effects become important and because the Euler–IBLT method uses a mechanical-energy formulation for the boundary layer, the obtained values of viscous dissipation are expected to be different than the RANS values. The overprediction of the isolated fuselage surface dissipation value [leading to a lower $((\dot{E} - P_V)/DV_\infty)_{TE}$] at higher Mach numbers and the overprediction of $\text{PSC}_{\text{strict}}$ for different cases in the Euler–IBLT solver must be more carefully analyzed on the basis of validity of the assumptions (like the thin boundary-layer assumption) and modeling details in the solver. However, unlike surface dissipation (or surface anergy generation rate) and the propulsive power, the effect of fuselage design (or flight condition) on BLI power saving (indicated by PSC values in Fig. 21) is not very interesting, as the changes (with respect to the baseline value) involved are small compared to the changes in power-related terms (like surface dissipation, surface anergy, and propulsive power). For example, even if the flight Mach is changed from 0.2 to 0.8, the change in PSC values is much smaller when compared to the change in the fuselage surface dissipation.

Next, the r50 propulsor effectively uses the BLI benefit as observed from the $\text{PSC}_{\text{strict}}$ value, which is closer to the maximum isolated body exergy flow. The Mach 0.9 and the fuselage slenderness of 5 cases have a high amount of exergy flow in thermal form (also shown in Fig. 21), and thus, the propulsor performance

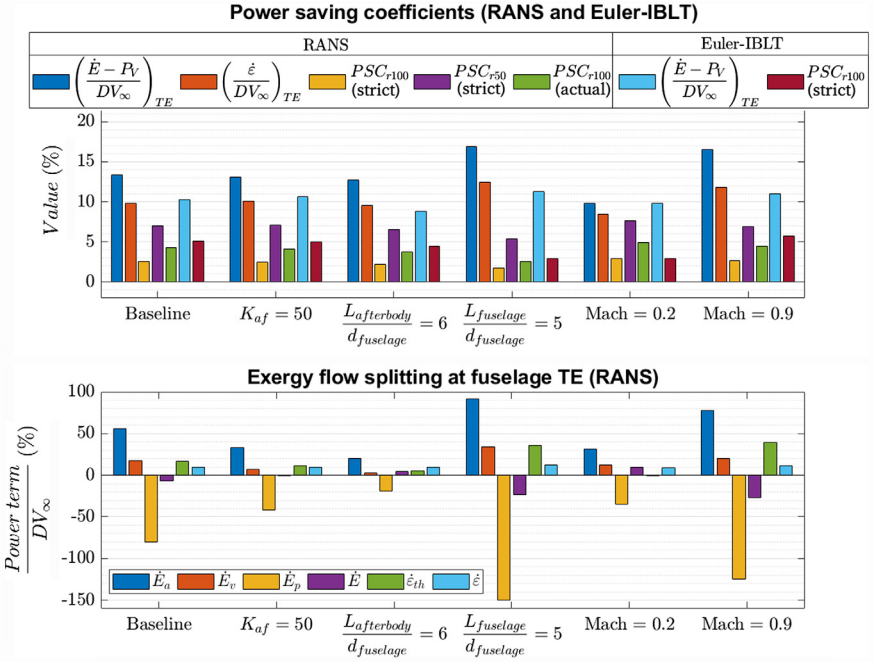

Fig. 21 Summary of PSC results (RANS and Euler–IBLT); the $\dot{E} - P_V$ and $\dot{\varepsilon}$ terms represent the PSC_{ideal} values based on PBM and EAM, respectively.

deteriorates (resulting in higher difference between PSC_{ideal} and PSC_{strict} values). On the whole, the respective PSC (ideal, strict, and actual) values change only by a small amount for the different cases of fuselage design or flight conditions. The case with a fuselage slenderness of 5 has a little bit higher exergy flow at the fuselage TE, as the laminar flow contributes to a significant portion of the boundary-layer anergy generation rate (which is lesser than that of the turbulent flow) as the fuselage is short. The Mach 0.9 case also has a little bit higher exergy flow rate at fuselage TE. It is nevertheless clear that the changes to the fuselage design or flight speed have a higher effect on the theoretical requirement for propulsion (based on fuselage surface anergy rate) than on BLI power benefit [indicated by PSC_{ideal} (isolated), PSC_{strict} (BLI), and PSC_{actual} (BLI) values]. Finally, the fuselage surface anergy rate was not changed significantly (<1% changes) by adding the propulsor in the aft for all the cases.

Furthermore, the flowfields (Mach and static pressure coefficient) for the baseline fuselage case with and without the propulsor for Euler–IBLT and RANS simulations are given in Fig. B1 in Appendix B. The similarity between the methods for inviscid flowfield can be observed. The complete boundary-layer flowfield is not available from the Euler–IBLT solver, and only certain integral quantities and boundary-layer edge quantities are obtained, which are useful for calculating certain PBM terms. Apart from this, the flowfields from

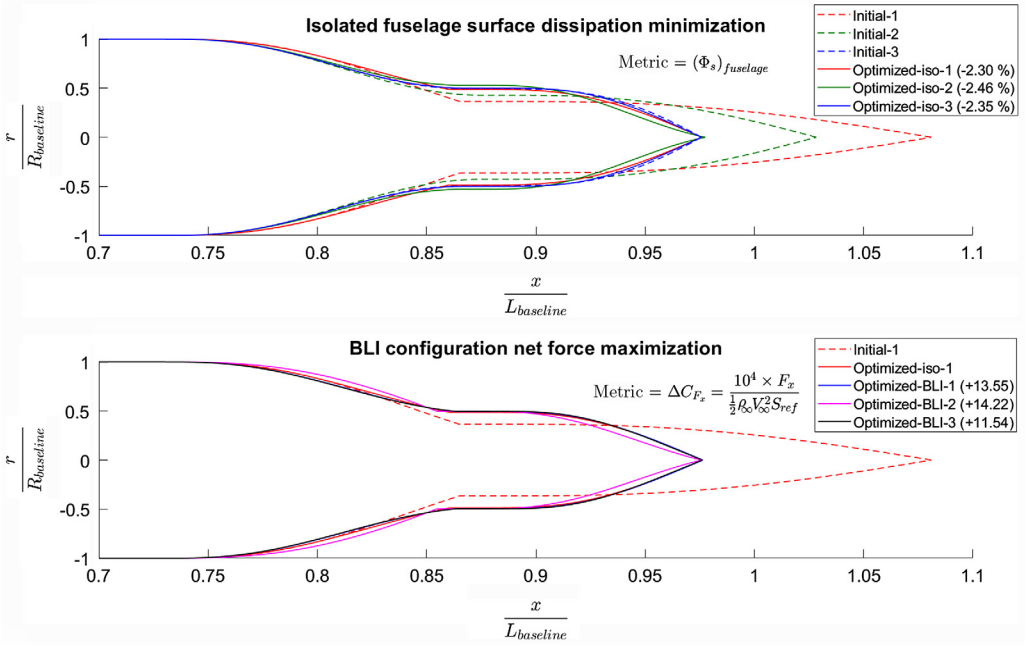

Fig. 22 Optimization results using Euler–IBLT solver (zoomed view); the change in metric value is mentioned in the legend for each run.

the RANS simulations for the cases of fuselage with different propulsor sizes located at the fuselage TE and at a distance of $L_{\text{fuselage}} - 0.75L_{\text{afterbody}}$ are given in Figs. B2 and B3, respectively. The difference in the filling of boundary layer can be observed for the different cases.

Lastly, it should be noted that the present study uses an axisymmetric model for the simulations. The circumferential flow distortions are an important aspect to consider for BLI applications [16]. Especially, it is easy to understand that this would affect the turbomachinery performance, and thus, future studies should include nonaxisymmetric flows (not possible in the present Euler–IBLT solver) and a higher-fidelity model of the propulsor. In any case, the PSC trends are not expected to change much for slightly nonaxisymmetric cases for the propulsor model used in the present study. This is because the PSC values did not change for a wide range of designs involving much-higher pressure gradient changes than would be caused by slight nonaxisymmetric flow.

C. Fuselage Afterbody Optimization

A gradient-based optimization is performed using the Euler–IBLT solver. The isolated and powered fuselage configurations are optimized separately. For the isolated fuselage, the minimization of the isolated fuselage surface viscous dissipation is performed. Three different initial geometries are implemented. For the powered configuration, the maximization of the net axial force for a fixed propulsor power is performed. Three different initial values of the net force are used as initial conditions. These include a net force equal to zero, a net force equal to the baseline isolated fuselage body drag, and a net force equal to twice the baseline isolated fuselage drag. This is done to make sure that the effect of the propulsor jet on the viscous dissipation in downstream fuselage boundary layer is accounted for in the optimization study. The radial propulsor dimension is fixed such that the inlet cross-sectional area equals that of a circle with 1.25 times the baseline fuselage radius.

The optimized fuselage afterbody shape is almost the same in all trails (with and without a BLI propulsor). Figure 22 shows a zoomed view of the afterbody geometries in the optimization study. The dissipation and net force count change is also mentioned for each optimized geometry. It can be observed that the value of fuselage surface dissipation does not change much for the three geometries in the isolated fuselage dissipation minimization study. On the other hand, the result for the BLI configuration net force maximization case, there is a minor difference in the net force count increase (a quantity 21 defined similar to drag count) between the optimized geometries. It can be observed that the second optimized geometry (optimized-BLI-2) has the highest net force increase in spite of having to maintain a higher initial net force (and hence higher PR) compared to the first (optimized-BLI-1). It should be noted that the decrease in fuselage surface area downstream of the propulsor could lead to a lesser increase in viscous dissipation downstream of the propulsor (due to the exhaust interacting with the boundary layer). However, the optimized-BLI-3 clearly has a lower force count increase, possibly due to the high initial PR. This again indicates the possibility that extra viscous losses could occur due to the exhaust interacting with the boundary layer (as observed in the propulsor position design space exploration study). Finally, it is observed that the differences in fuselage drag values (for the given Mach) between all the optimized fuselage geometries (in both the optimizations) are less than 1%.

VI. Conclusions

The current work involved the aeropropulsive performance analysis of fuselage BLI. A design space study was carried out to analyze the performance of different fuselage designs (and flight conditions). An Euler–IBLT solver was used for the design space study, and the results for the selected cases were validated using RANS simulations. The Euler–IBLT solver was found to give similar qualitative results as the RANS solver for the design space study. Moreover, the Euler–IBLT solver also splits the computational domain into a viscous and an inviscid part, allowing for the explicit understanding of viscous effects unlike the RANS solver. This is especially useful when the propulsor is positioned upstream of the fuselage TE, as it allows for the direct calculation of the viscous dissipation along with the interaction effect of the propulsor jet (on the boundary layer). The RANS solver, on the other hand, does not allow for such an explicit separation of the dissipation in the fuselage boundary layer (along with propulsor jet interaction) and the propulsor jet alone. However, the RANS solver allows for the utilization of both the PBM and the EAM, unlike the Euler–IBLT solver where only the PBM is applicable.

Next, the results of the design space exploration show the following:

1) The effect of the fuselage design (and the flight speed) on the BLI power benefit is much lower when compared to the effect on the isolated fuselage drag power. Thus, the fuselage performance for BLI configurations is comparable on a qualitative basis using the isolated body drag value itself.

2) The surface dissipation is an important parameter for comparing the performance of different fuselages. However, the surface anergy rate is more appropriate (especially in compressible conditions) to quantify the possible theoretical BLI benefit (using an isolated body analysis) as it accounts for the thermal effects. This suggests that the RANS studies using EAM are more important than the Euler–IBLT studies, where only PBM is applicable.

3) In case of the fuselage body extending downstream of the BLI propulsor, the results suggest that the interaction of the propulsor jet with the boundary layer could increase the local surface dissipation. However, the fuselage surface dissipation (as mentioned in previous studies in the literature) and the anergy generation rate upstream of the propulsor are unaffected.

4) Qualitatively, the variation in the fuselage surface dissipation (expected based on studies in the literature) and the surface anergy generation rate for the range of fuselage designs and flight conditions analyzed is similar to that of the propulsor power consumption in BLI configurations. Also, the power saving results from PBM and EAM in the isolated fuselage RANS studies show similar qualitative trends for the different fuselage geometries and flight speeds considered.

The findings of this study should be further assessed in future studies to take into account the actual propulsor design (by using higher-fidelity models) and the effects of nonaxisymmetric inflow conditions.

Appendix A: Fuselage Afterbody Shape

The fuselage forebody and afterbody shapes have been defined based on the ESDU I and ESDU II curve families, respectively, as defined in the ESDU 77028 document [28]. The ESDU I curve family is defined by the equations:

$$\frac{r}{R} = \frac{\sqrt{\alpha_1}}{8}(15 - 10\alpha_1 + 3\alpha_1^2) \tag{A1}$$

$$\alpha_1 = \frac{\left[\frac{x}{L} + K_{\text{fo}}\left[\frac{x}{L}\right]^2\right]}{1 + K_{\text{fo}}} \tag{A2}$$

Next, the ESDU II curve family is defined by the equations:

$$\frac{r}{R} = \alpha_2(3 - 3\alpha_2 + \alpha_2^2) \tag{A3}$$

$$\alpha_2 = \frac{\left[\frac{x}{L} + K_{\text{af}}\left[\frac{x}{L}\right]^2\right]}{1 + K_{\text{af}}} \tag{A4}$$

In the preceding equations, R refers to the maximum radius of the body under consideration, and L refers to the length of the body.

Appendix B: Flowfields

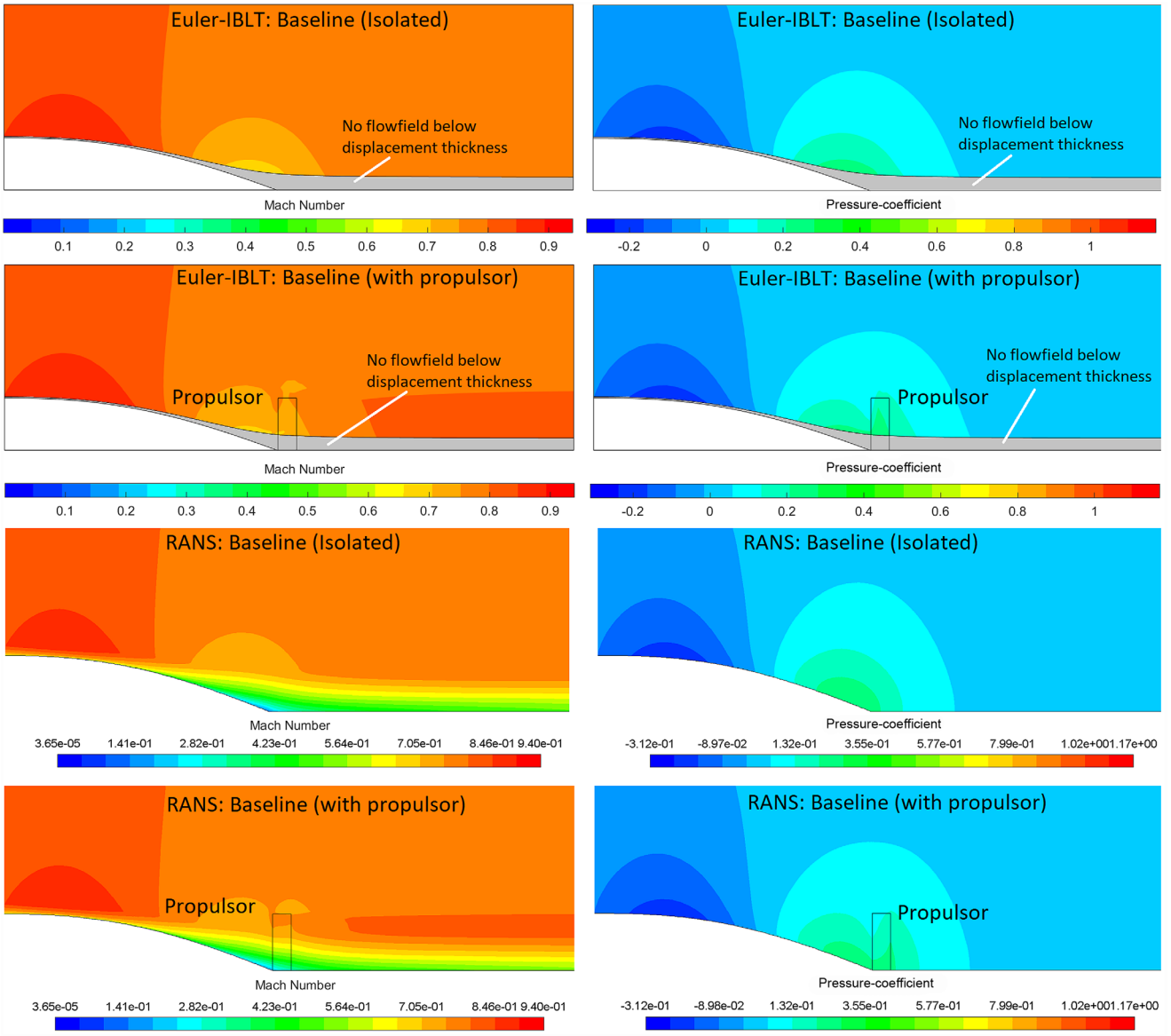

Fig. B1 Flowfields near fuselage afterbody (Euler–IBLT and RANS) for baseline fuselage; $F_x = D$ (for isolated); $F_x = 0$ (for installed); $M = 0.8$.

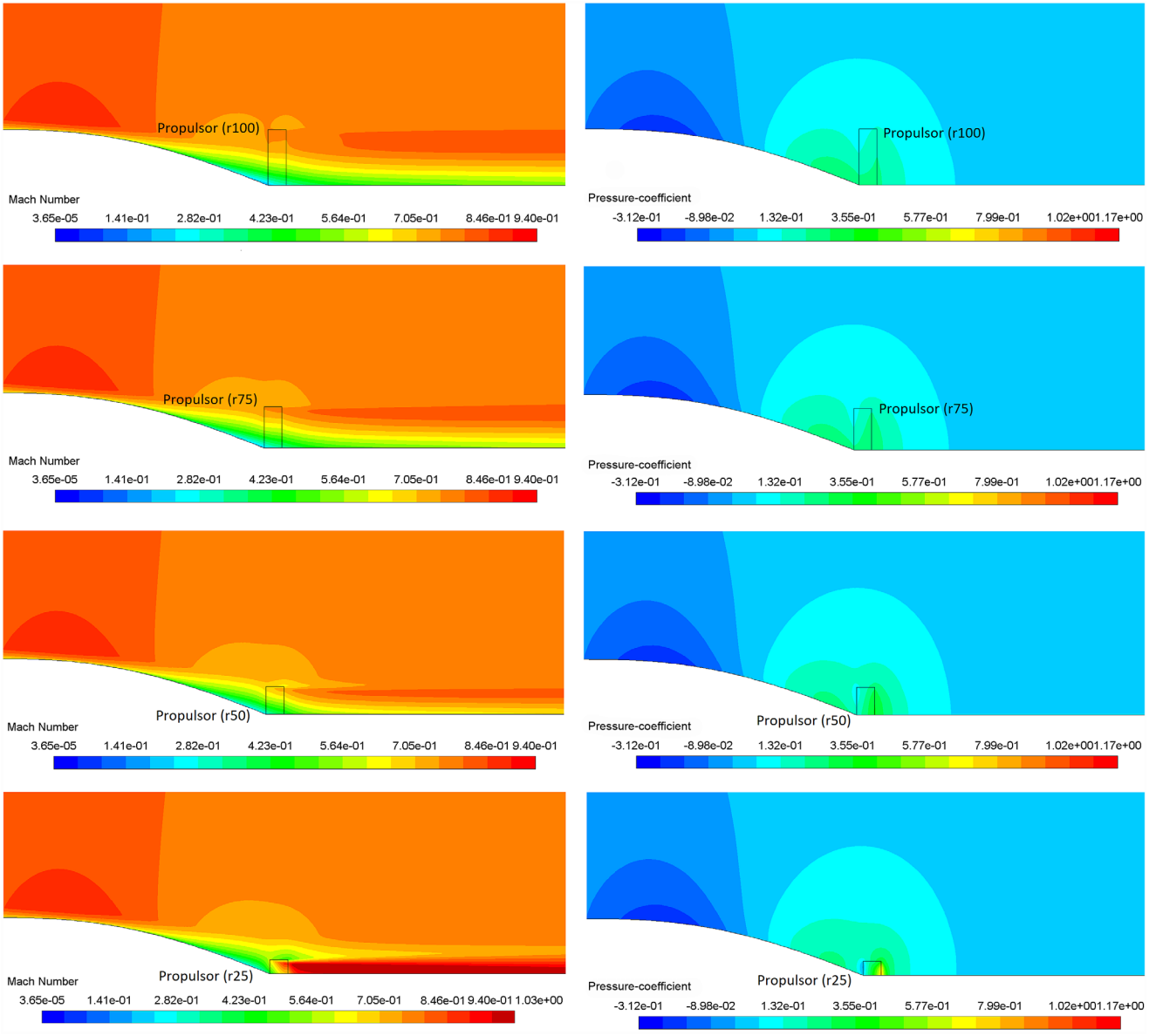

Fig. B2 Flowfields near fuselage afterbody (RANS) for different propulsor radii and a fixed propulsor position at fuselage TE; $F_x = 0$; $M = 0.8$.

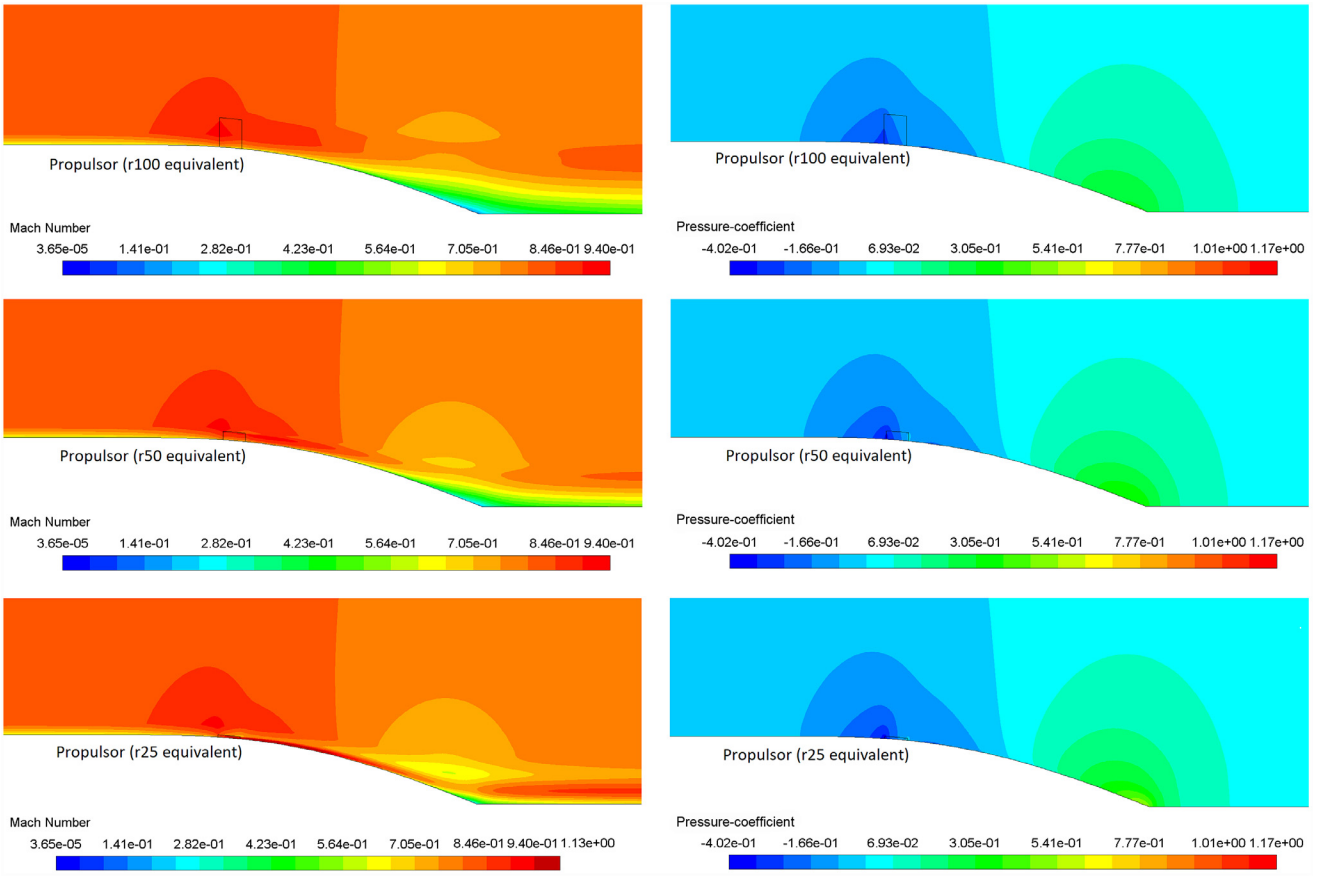

Fig. B3 Flowfields near fuselage afterbody (RANS) for different propulsor radii and a fixed propulsor position of $L_{\text{fuselage}} - 0.75L_{\text{afterbody}}$ from the fuselage leading edge; $F_x = 0$; $M = 0.8$.

References

[1] Ashcraft, S. W., Padron, A. S., Pascioni, K. A., Stout, G. W., Jr., and Huff, D. L., "Review of Propulsion Technologies for N+3 Subsonic Vehicle Concepts," NASA TM-2011-217239, Oct. 2011, https://ntrs.nasa.gov/citations/20110022435.

[2] European Commission, "Flightpath 2050, Europe's Vision for Aviation," Report of the High Level Group on Aviation Research, Publications Office of the European Union, Luxembourg, 2012. https://doi.org/10.2777/15458

[3] Smith, L. H., "Wake Ingestion Propulsion Benefit," *Journal of Propulsion and Power*, Vol. 9, No. 1, 1993, pp. 74–82. https://doi.org/10.2514/3.11487

[4] Isikveren, A. T., Seitz, A., Bijewitz, J., Mirzoyan, A., Isyanov, A., Grenon, R., Atinault, O., Godard, J. L., and Stückl, S., "Distributed Propulsion and Ultra-High By-Pass Rotor Study at Aircraft Level," *Aeronautical Journal*, Vol. 119, No. 1221, 2015, pp. 1327–1376. https://doi.org/10.1017/S0001924000011295

[5] Uranga, A., Drela, M., Greitzer, E. M., Hall, D. K., Titchener, N. A., Lieu, M. K., Siu, N. M., Casses, C., Huang, A. C., Gatlin, G. M., and Hannon, J. A., "Boundary Layer Ingestion Benefit of the D8 Transport Aircraft," *AIAA Journal*, Vol. 55, No. 11, 2017, pp. 3693–3708. https://doi.org/10.2514/1.J055755

[6] Atinault, O., Carrier, G., Grenon, R., Verbecke, C., and Viscat, P., "Numerical and Experimental Aerodynamic Investigations of Boundary Layer Ingestion for Improving Propulsion Efficiency of Future Air Transport," *31st AIAA Applied Aerodynamics Conference*, AIAA Paper 2013-2406, June 2013. https://doi.org/10.2514/6.2013-2406

[7] Lv, P., Rao, A. G., Ragni, D., and Veldhuis, L. L. M., "Performance Analysis of Wake and Boundary-Layer Ingestion for Aircraft Design," *Journal of Aircraft*, Vol. 53, No. 5, 2016, pp. 1517–1526. https://doi.org/10.2514/1.C033395

[8] McCormick, B., and Elsenuth, J., "Design and Performance of Propellers and Pumpjets for Underwater Propulsion," *AIAA Journal*, Vol. 1, No. 10, 1963, pp. 2348–2354. https://doi.org/10.2514/3.2065

[9] Wislicenus, G. F., "Hydrodynamics and Propulsion of Submerged Bodies," *American Rocket Society Journal*, Vol. 30, No. 12, 1960, pp. 1140–1148. https://doi.org/10.2514/8.5351

[10] Betz, A., *Introduction to the Theory of Flow Machines*, Pergamon Press, Oxford, 1966, pp. 215–216.

[11] Habermann, A., Bijewitz, J., Seitz, A., and Hornung, M., "Performance Bookkeeping for Aircraft Configurations with Fuselage Wake-Filling Propulsion Integration," *Council of European Aerospace Societies Aeronautical Journal*, Vol. 11, No. 2, 2020, pp. 529–551. https://doi.org/10.1007/s13272-019-00434-w

[12] Drela, M., "Power Balance in Aerodynamic Flows," *AIAA Journal*, Vol. 47, No. 7, 2009, pp. 1761–1771. https://doi.org/10.2514/1.42409

[13] Lv, P., and Rao, A. G., "Conceptual Analysis of Boundary-Layer Ingestion Towards Aircraft Propulsion Integration," *21st International Symposium on Air Breathing Engines*, ISBAE Paper 2013-1436, Busan, South Korea, June 2013, https://www.researchgate.net/publication/260433892_Conceptual_Analysis_of_Boundary_Layer_Ingestion_Towards_Aircraft_Propulsion_Integration [retrieved 11 March 2021].

[14] Lv, P., Ragni, D., Hartuc, T., Veldhuis, L. L. M., and Rao, A. G., "Experimental Investigation of the Flow Mechanisms Associated with a Wake-Ingesting Propulsor," *AIAA Journal*, Vol. 55, No. 4, 2016, pp. 1332–1342. https://doi.org/10.2514/1.J055292

[15] Arntz, A., Atinault, O., and Merlen, A., "Exergy-Based Formulation for Aircraft Aeropropulsive Performance Assessment: Theoretical Development," *AIAA Journal*, Vol. 53, No. 6, 2014, pp. 1627–1639. https://doi.org/10.2514/1.J053467

[16] Kenway, G. K., and Kiris, C. C., "Aerodynamic Shape Optimization of the STARC-ABL Concept for Minimal Inlet Distortion," *2018 AIAA/ASCE/AHS/ASC Structures, Structural Dynamics, and Materials Conference*, AIAA Paper 2018-1912, 2018. https://doi.org/10.2514/6.2018-1912

[17] Plas, A., Crichton, D., Sargeant, M., Hynes, T., Greitzer, E., Hall, C., and Madani, V., "Performance of a Boundary Layer Ingesting (BLI) Propulsion System," *45th AIAA Aerospace Sciences Meeting and Exhibit*,

AIAA Paper 2007-0450, Jan. 2007.
https://doi.org/10.2514/6.2007-450

[18] Gunn, E., and Hall, C., "Aerodynamics of Boundary Layer Ingesting Fans," *Turbo Expo: Power for Land, Sea, and Air*, Vol. 45578, American Soc. of Mechanical Engineers, Fairfield, NJ, 2014, p. V01AT01A024. https://doi.org/10.1115/GT2014-26142

[19] Kim, H., and Felder, J., "Control Volume Analysis of Boundary Layer Ingesting Propulsion Systems with or Without Shock Wave Ahead of the Inlet," *49th AIAA Aerospace Sciences Meeting Including the New Horizons Forum and Aerospace Exposition*, AIAA Paper 2011-222, 2011. https://doi.org/10.2514/6.2011-222

[20] Sabo, K. M., and Drela, M., "Benefits of Boundary Layer Ingestion Propulsion," *53rd AIAA Aerospace Sciences Meeting*, AIAA, Reston, VA, 2015.
https://doi.org/10.2514/6.2015-1667

[21] Gray, J. S., Mader, C. A., Kenway, G. K., and Martins, J., "Approach to Modeling Boundary Layer Ingestion Using a Fully Coupled Propulsion-RANS Model," *58th AIAA/ASCE/AHS/ASC Structures, Structural Dynamics, and Materials Conference*, AIAA Paper 2017-1753, 2017. https://doi.org/10.2514/6.2017-1753

[22] Elmiligui, A. A., Fredericks, W. J., Guynn, M. D., and Campbell, R. L., "Numerical Investigation of a Fuselage Boundary Layer Ingestion Propulsion Concept," *2013 Aviation Technology, Integration, and Operations Conference*, AIAA Paper 2013-4402, 2013. https://doi.org/10.2514/6.2013-4402

[23] Blumenthal, B., Elmiligui, A. A., Geiselhart, K., Campbell, R. L., Maughmer, M. D., and Schmitz, S., "Computational Investigation of a Boundary Layer Ingestion Propulsion System for the Common Research Model," *46th AIAA Fluid Dynamics Conference*, AIAA Paper 2016-3812, June 2016.
https://doi.org/10.2514/6.2016-3812

[24] Baskaran, P., "Aero-Propulsive Performance Analysis of Fuselage for Boundary Layer Ingestion," Master's Thesis, Delft Univ. of Technology, Delft, The Netherlands, 2019 (unpublished), http://resolver.tudelft.nl/uuid:97511baf-3e8b-4673-aa76-a4cd5330bd36 [retrieved 11 Aug. 2021].

[25] Moore, J., and Moore, J. G., "Entropy Production Rates from Viscous Flow Calculations: Part I—A Turbulent Boundary Layer Flow," *ASME 1983 International Gas Turbine Conference and Exhibit*, American Soc. of Mechanical Engineers, Fairfield, NJ, 1983, p. V001T01A032. https://doi.org/10.1115/83-GT-70

[26] Hall, D. K., Huang, A. C., Uranga, A., Greitzer, E. M., Drela, M., and Sato, S., "Boundary Layer Ingestion Propulsion Benefit for Transport Aircraft," *Journal of Propulsion and Power*, Vol. 33, No. 5, 2017, pp. 1118–1129. https://doi.org/10.2514/1.B36321

[27] Stokkermans, T. C. A., van Arnhem, N., and Veldhuis, L. L. M., "Mitigation of Propeller Kinetic Energy Losses with Boundary Layer Ingestion and Swirl Recovery Vanes," *Proceedings of the 2016 Applied Aerodynamics Research Conference*, Royal Aeronautical Soc., London, July 2016, pp. 56–69.

[28] Chappell, P. D., Clarke, A., Porter, R., and Wood, S. F., "Geometrical Characteristics of Typical Bodies," *IHS ESDU*, Vol. 77028, Nov. 1977, https://www.esdu.com/cgi-bin/ps.pl?sess=unlicensed_1211103212717pvq<=doc>=esdu_77028g [retrieved 11 Aug. 2021].

[29] Drela, M., "A User's Guide to MTFLOW 2.01," June 2010, http://web.mit.edu/drela/Public/web/mtflow/mtflow.pdf [retrieved 11 Aug. 2021].

[30] Drela, M., "Two-Dimensional Transonic Aerodynamic Design and Analysis Using the Euler Equations," Ph.D. Thesis, Massachusetts Inst. of Technology, Cambridge, MA, 1986.

[31] Menter, F. R., "Two-Equation Eddy-Viscosity Turbulence Models for Engineering Applications," *AIAA Journal*, Vol. 32, No. 8, 1994, pp. 1598–1605.
https://doi.org/10.2514/3.12149

[32] Spalart, P. R., and Rumsey, C. L., "Effective Inflow Conditions for Turbulence Models in Aerodynamic Calculations," *AIAA Journal*, Vol. 45, No. 10, 2007, pp. 2544–2553.
https://doi.org/10.2514/1.29373

[33] Stokkermans, T. C., Arnhem, N. V., Sinnige, T., and Veldhuis, L. L. M., "Validation and Comparison of RANS Propeller Modeling Methods for Tip-Mounted Applications," *2018 AIAA Aerospace Sciences Meeting*, AIAA Paper 2018-0542, Dec. 2018.
https://doi.org/10.2514/6.2018-0542

[34] Seitz, A., Peter, F., Bijewitz, J., Habermann, A., Goraj, Z., Kowalski, M., Castillo, A., Meller, F., Merkler, R., Samuelsson, S., et al., "Concept Validation Study for Fuselage Wake-Filling Propulsion Integration," *31st Congress of the International Council of the Aeronautical Sciences*, ICAS Belo Horizonte, Brazil, 2018, pp. 9–14, https://www.icas.org/ICAS_ARCHIVE/ICAS2018/data/papers/ICAS2018_0342_paper.pdf [retrieved 11 Aug. 2021].

[35] Chappell, P. D., and Wood, S. F., "Profile Drag of Axisymmetric Bodies at Zero Incidence for Subcritical Mach Numbers," *IHS ESDU*, Vol. 78019, July 1978, https://www.esdu.com/cgi-bin/ps.pl?sess=unlicensed_1211103215001cyj<=cdoc>=cdoc_esdu78019 [retrieved 11 Aug. 2021].

F. Grasso
Associate Editor